Politecnico di Torino

Dipartimento di Ingegneria Meccanica e Aerospaziale

Laurea Magistrale in Ingegneria Aerospaziale

Master Thesis

Investigation of Field Decomposition Methods for Simulations of Turbulent Flow Grazing an Acoustic Liner

Supervisor:

Prof. Renzo Arina

Candidate:

Oleksiy Kovalenko

Co-Supervisor:

Angelo Paduano

Francesco Scarano

Politecnico di Torino

2022-2023

Acknowledgements

"Computational resources were provided by HPC@POLITO, a project of Academic Computing within the Department of Control and Computer Engineering at the Politecnico di Torino (http://hpc.polito.it)"

Abstract

The subject of this thesis focuses on the study, analysis, and current challenges of recently introduced methods for flow field analysis and decomposition, namely Spectral Proper Orthogonal Decomposition (SPOD) and Wavelet Transform (WT). Spectral POD is a decomposition technique designed to identify energy-ranked modes within a flow field, where each mode corresponds to a specific frequency, allowing for the distinctive separation of phenomena occurring at different frequencies and energy levels. Wavelet transform is another powerful method for analysing signals in both time and frequency domains, by decomposing a signal into different scales with the use of wavelet functions, it provides a localized representation of signal features, making it suitable for detecting transient events or localized variations, like identifying coherent structures and turbulence study. The main topic is the application of these promising techniques to a numerical simulation of a turbulent flow grazing acoustic liners, which purpose is damping acoustic energy travelling a duct or a pipe. Acoustic liners exhibit diverse behaviours in response to the different conditions, such as incident waves' sound pressure level, frequency, or presence of a mean flow. Bearing in mind that modal analysis or proper filtering procedures can be used to decompose the pressure signal into acoustic and hydrodynamic components, which present different peculiarities, SPOD and WT are supposed capable of identifying these components for a deeper understanding of the underlying physics. The forementioned techniques, being very computational power demanding, became available for practical situations only with recent technological achievements, for this reason, HPC computational resources offered by Politecnico di Torino are used to analyse acoustic liners functioning in different characterizing conditions. The results are used firstly to identify the various functioning regimes of single degree-of-freedom acoustic liners, and after adopted to investigate whether is possible a separation of acoustic and hydrodynamic components of the resulting flow field. After a brief introduction of the main topics, an appropriate description of the used methods, algorithms, and flow conditions analysed is reported, key parameters and experimental setup is described right after and finally main results and outcomes are presented.

Contents

Nomenclature

Symbols

$\mathbb{S}$	Cross Spectral Density (tensor)
$\mathbf{x}$	fluctuating part of a generic variable
a	expansion coefficient realtive to the extracted mode
i	imaginary unit
N_b	number of blocks in wich is subdivided a data series
N_f	number of snapshots (or frames) forming a block
N_T	total number of snapshots, of wich consist a data series
N_{of}	offset number of frames (snapshot that are removed
N_{ov}	number of ovelapping frames, snapshots by which two adjacent blocks are overlapping
p'	pressure fluctuation
W	weight matrix
dB	decibel
T	generic period

Greek Symbols

λ	generic eigenvalue
ϕ	generic mode

Superscripts

$\overline{(\cdot)}$	mean value

$\tilde{(\cdot)}$	elements obtained by a distretized approach that mimic the theoretical result

Subscripts

rms	root mean square

Acronyms / Abbreviations

full	the first SPOD ROI, analyzing the whole flow field domain with "great" resources demanding workload
inlet	duct section before the liners array area
liners	liners cavities area
main	duct section "under" the liners array
orifices	11 square areas comprehending only the orifices of each liner
outlet	duct section after the liners array region
BPF	Blade Passing Frequency
CSD	Cross Spectral Density (tensor)
CWT	Continuous Wavelet Transform
DWT	Discrete Wavelet Transform
HVAC	Heat Ventilation & Air Conditioning
PCA	Principal Component Analysis
POD	Proper Orthogonal Decomposition
ROI	Region of Interest
SDOF, DDOF	Single Degree-Of-Freedom, Double Degree-Of-Freedom
SPL	Sound Pressure Level
SPOD	Spectral Proper Orthogonal Decomposition

Introduction

1.1 Problem description

In every physic phenomenon, it is important to fully understand its origin and quantify the contribution of different sources to its generation. The generation of sound is a topic of interest in various fields, such as aerospace, automotive, civil engineering and others, and common applications that include a moving fluid define the aeroacoustics study and analysis, such as aircraft and vehicle generated noise, heat ventilation & air conditioning (HVAC) systems and many others. A common practice to theoretically and numerically study the generation and suppression of sound in the case of a moving fluid is to use an acoustic analogy [29, 12, 8], and to obtain the radiated sound in the region of interest (ROI), the time-dependent flow field solution in the source region is required. For generic model problems, the flow field can be given by analytic functions based on assumptions on homogeneous turbulence [20]. For more complex flows, time-dependent solutions of equations as non-linear Euler or Navier–Stokes need to be obtained numerically[1], with increasing computational power, the possibility of overcome intrinsic difficulties such as very fine computational mesh, suitably large computational domain or high-order accurate time marching computational scheme has increased greatly [1], but remains unfeasible for design purposes.

An alternative approach is to investigate and identify the main elements that characterize and influence the entire flow field and its acoustic behavior, by decomposing the flow field resulting from an experimental setup. Hence, a distinction between *sound* and *pseudo-sound* can be made in the near field of an aeroacoustic source. The sound or acoustic component is associated with sound waves propagating at the speed of sound and governed by the linear wave equation, while the pseudo-sound, also called the hydrodynamic component, is weakly influenced by compressibility and does not radiate [12]. It results

[1] In a Direct Numerical Simulation (DNS), the non-linear Navier–Stokes equations are solved numerically, yielding time-dependent data of e.g. the pressure and velocity field. However, it can be difficult to clearly isolate and identify the sound generating structures in the solution. Furthermore, performing DNS at realistic Reynolds numbers is computationally expensive, and the amount of raw data produced is large enough such that storage becomes an issue. The same issues also hold for Large Eddy Simulations (LES) or Detached Eddy Simulations (DES).

of interest of scientific community efficiently distinct and analyze separately the two components. Such a separation could be achieved by a proper filtering procedure[2], since the hydrodynamic component is dominant in the low-frequency region of the spectrum, whereas the acoustic component is predominant at high frequencies [27, 52]. Difficulty stems from the fact that only a small part of the energy associated with the pressure fluctuations radiates as sound, and e.g. in the vicinity of a jet, the pressure field is dominated by the pseudo-sound, but this contribution decays very rapidly, and at large distances, the pressure field reduces solely to the acoustic one [20]. When a measurement of fluctuating pressure is performed in the near field, the acoustic contribution is buried by the hydrodynamic contribution, and it is indistinguishable with a single microphone signal. The problem of decomposing the whole signal into acoustic and hydrodynamic pressure can be overcome through the modal analysis or application of a proper filtering procedure[3].

1.2 Acoustic liners

Since the beginning of the modern aviation, aircraft's noise emission has been one of the main topics, and one of the effectively adopted techniques for reducing derived noise is the installation of acoustic liners, being introduced since the early 1950s [21], they rely on the concept of the Helmholtz resonators disposed in an array to absorb acoustic energy from the incoming flow. Among several peculiarities, these are passive devices, hence, by selecting proper design parameters they can absorb acoustic energy from waves travelling along surfaces on which these liners are installed, such as tonal noise generated by the fan or a more complex broadband noise due to turbulent flow resulting in specific regions. When the facing flow contains acoustic waves within certain levels, noise is damped via thermal and viscous losses within the orifices in the face-sheet [36]; but in the case of sound pressure levels greater than a threshold, acoustic energy is converted into vorticity by vortex shedding at the edges of the orifices [36]. Acoustic liners are effective absorbers in a narrow frequency band [5] which depends on geometrical design parameters, but, under certain conditions, they can provide noise mitigation in a sufficiently broad range.

[2] A Fourier filtering procedure for the separation of hydrodynamic and acoustic pressures in the near field was presented by Kerhervé et al. (2008) and Tinney & Jordan (2008). Pseudo-sound and sound pressures were isolated because of their phase velocity in the wave number–frequency spectrum. Even though these results are encouraging, it must be pointed out that the use of Fourier-based filters can lead to an incomplete description of the acoustic near field. Indeed, the use of high-pass or low-pass filters implies that properties of sound at low frequencies and of pseudo-sound at high frequencies are filtered out and thus are definitely lost.

[3] Indeed, Arndt et al. (1997) and Coiffet et al. (2006) proposed an ad hoc separation of the near-field pressure spectra into a low-frequency hydrodynamic region and a high-frequency acoustic region. They definitely suggested that a separation between sound and pseudo-sound can be achieved by a low-pass or high-pass filter of the data.

This happens, for example, with high-amplitude incident sound waves, or the presence of a flow, for which the liners present a non-linear behavior. Under these conditions, vortex shedding occurs in the orifices on the face-sheet and the Reynolds number (Re) regulates the frequency range of acoustic energy reduction [51]. This setup is known as Single DOF (degree-of-freedom) while the addition of a porous septum inside the cavity, simulating two cavities in series, allows a second absorption peak and a broader frequency range of noise dampening, in this case, the system is referred to as *Double* DOF [36].

Continuous technological developments have permitted to alleviate the dominant source's contribution to overall noise generation, causing the main noise component to shift from a single tone to a broadband emitter. As a result, acoustic liners are now needed to absorb sound over a wide frequency range, preferably up to at least two octaves [24]. Several investigations have been conducted in order to demonstrate the effectiveness of liners for acoustic damping, e.g. optimization studies conducted on constructive parameters of lined flaps for trailing edge noise reduction [5], and in recent years, leading aircraft engine manufacturers adopted this technology to comply with the most recent aircraft noise emission regulations concerned for future environmental impact like the single-layer and double-layer liners with perforations and mesh facing sheets adopted on the latest models of Rolls-Royce turbofan engines [26]. Furthermore, liner technology is constantly being studied for noise reduction of aircraft broadband sources [40, 41].

The key for optimal performance (minimal impact on aerodynamic characteristics) is the sizing, design and distribution of the cavities and holes on the surfaces facing the grazing flow containing acoustic waves, hence to increase the acoustic energy absorption and a more profound understanding of the implied physics, more studies are necessary. Valuable data of the flow fields produced in the presence of acoustic waves travelling through the ducts and their interaction with liners in different conditions can be obtained from experimental setups or through numerical simulations. Fluid dynamic fields data, nowadays, can reach a very high level of definition, limited only by the computational power available, it follows that appropriate analysis methods are needed to effectively and methodically inspect these data.

1.3 Flow Field decomposition techniques

There are available several techniques which allow to successfully decompose and analyze a flow field, and the common step for the most promising of them relies on a shift of domain such as Fourier or Wavelet transform, allowing this way a deep inspection of the underlying dynamics.

Modal decomposition is a mathematical technique for extracting energetically and dynamically important features from some sort of data, and in particular out of fluid flows. The extracted coherent features, called modes, can be used to acquire insight into the underlying physics of the particular phenomenon; these modes are accompanied by characteristic values that represent either the energy content levels, the growth rates, or frequencies. In fluid dynamics, these modes can be determined from the flow field data or from the governing equations, and in case the flow field data is used as input, these analyses are called *data-based* techniques [34, 50] while the seconds are usually referred to as *operator-based* techniques; meaning that, *data-driven* techniques, such as *Proper Orthogonal Decomposition* (POD), do not require knowledge of the governing equations to extract valuable data. POD is one of the most adopted methods in fluid dynamics, and it is available with several variations to exploit particular features or domain of coherent structures of the examined situation e.g. *Space* or Standard, *Spectral*, *Balanced* and many others [50].

Proper Orthogonal Decomposition (POD) outputs modes based on optimizing the mean square of the field variable being examined. It was introduced to the fluid dynamics and turbulence study community by Lumley [34] as a mathematical technique to extract coherent structures from turbulent flow fields. The POD technique is also known as the Karhunen-Loève method, principal component analysis (PCA), Hotelling analysis etc. depending on the field of adoption; it provides an algorithm to decompose a set of data into a minimal number of basis functions or modes that represent the set of coherent structures with own energy levels involved. POD modes are by definition orthogonal and hierarchically ordered regarding their energetic contribution. Since this, the POD method (and its variations) appears to be well suited for turbulence and coherent structures dynamics analysis. Space-only POD Determines low-rank approximations based on modes orthogonal only-in-space and each mode is related to several frequencies, while Spectral POD (SPOD) extracts modes that vary in space and time and are orthogonal under a space-time inner product, and consequently resulting optimal in expressing data's coherence in both space and time. As a consequence, they can be associated to single frequencies, excelling, this way, in extracting coherent structures in experimental, turbulent and statistically stationary data (meaning that the mean and variance do not change in time). Mathematically, SPOD modes are the eigenvectors of a *Cross-Spectral Density* (CSD) tensor at each frequency.

In contrast to the modal analysis offered by the use of classical statistical tools, an alternative and also novel approach is offered through wavelet-transform based techniques [44] which do not require hypotheses such as the stationarity and homogeneity of the flow, meaning that also intermittent phenomenons can be represented as well, relying upon a representation utilizing analyzing functions, called *wavelets*, localized in space, and scaled before convolving with the signal for frequency inspection, resulting well localized in both

physical and frequency domain. Therefore, by filtering of such coefficients allows us to inspect different involved phenomenons preserving the spatial information, in opposition to Fourier modes, which are localized in the frequency domain and, for the record of the physical information, the phase of all coefficients is required. The continuous wavelet transform (CWT) offers a continuous and redundant unfolding in terms of both space and scale, which may enable us to track the dynamics of coherent structures and measure their contributions to the energy spectrum, while the discrete wavelet transform (DWT) allows an orthonormal projection on a minimal number of independent modes which might be used to compute or model the turbulent flow dynamics in a better way than with Fourier modes.

As Spectral POD and Wavelet transform seem well suited for inspection of coherent structures presence and contributions decomposition of the flow fields corresponding to acoustic liners, these novel techniques will be adopted in the course of this investigation work, but before investigating on whether SPOD or Wavelet transform could be valid analysis methods in characterizing acoustic field's dynamics and separating it from the hydrodynamic component, the next chapter will provide necessary background knowledge of the basic idea, the method's concept, the algorithm behind as well as differences, similarities, and advantages between *Spectral* and *Classic* (standard / space-only) POD, and the same introduction, reporting the key aspects and features, will be faced for the Wavelet Transform based decomposition as well.

1.4 Thesis objectives and structure

The idea that a flow field could be analyzed with proper attention on a particular aspect or mechanics is very attractive, as it could permit an easier and objective design study and investigation process, allowing immediate and reliable feedback from testing and analysis phases based on specific requirements and objectives. The examined study case is a perfect example where these recent methods could be the game changers for a more appropriate design characterization for acoustic noise control, where liners, to be defined by parametrization, require separate overview of aerodynamic and aeroacoustic damping performance.

The main objective of the current work is the investigation of whether is possible the characterization of certain phenomenons, their starting mechanics and dynamics by associating them to specific modes (or their combinations) through the use of Spectral Proper Orthogonal Decomposition and Wavelet transform for the analysis of flow fields resulting from numerically simulated turbulent flow grazing acoustic liners in a duct, in presence of acoustic waves, and possibly to determine a relation between generated structures responsible for noise absorption and the forementioned modes. The secondary

objective is the comparison of the selected modern techniques, relative feasibility, used parameters and detection of possible advantages or weaknesses, in terms of information delivered, for a better and properly selected aeroacoustic analysis technique, to be chosen in relation to the requested information of the specifically faced situation.

The thesis is structured as follows, the following chapter is dedicated to the required primary background information, functioning principles, theory, and design parameters of acoustic liners, modal decomposition techniques, with particular attention to POD, space-only and spectral, and Wavelets transform based methods. The simulation data processing details and methods, as well as defined parameters selection and setup adopted for the analyses, will be reviewed in the third chapter, the case study analysis results acquired by forementioned methods will be compared, organized and reviewed in chapter four. The concluding chapter will face and discuss any future outlooks as well as personal considerations and impressions.

Background and theory

2.1 Acoustic Liners

2.1.1 Generalities

The aeroacoustic noise generated by aircrafts in the vicinity of an airfield may be a great limitation to its regular operation, especially in urban and suburban areas. Aircraft noise emissions are regulated by international, regional, and local authorities, which is why manufacturers, designers, and researchers are constantly working to find new effective solutions to comply with these regulations and certify their products. The main acoustical sources on turbofan-powered aircraft are key components of the engine itself (fan, compressor, turbine, jet). The demand for greater efficiency and lower pollutant emissions has led aeronautical engine manufacturers to increase their engine bypass ratios, increasing this way on the one hand the fan size and the relative blade-passing-frequency (BPF) overall dominance and on the other hand the resulting broadband spread due to blade-stator flow interactions. Although many improvements have been made to reduce emitted noise, many difficulties stem from separating various contributions (especially at the aft end of a turbofan engine), effectively reducing one source's emission could be negligible or undistinguished from overall combined emission levels. One of the most adopted and effective solutions to achieve the desired levels of noise suppression in aircraft engines is the installation of acoustic liners in the intake, bypass, exit ducts and other wet surfaces that interact with the relevant flow contributing acoustically (Figure 2.1).

The main idea behind acoustic liners is to exploit the effectiveness of Helmholtz resonators, which consist of a chamber of relatively large volume (compared to the duct in which acoustic waves are propagating) with fluid under quiet conditions. At resonance frequencies, small pressure disturbances induce great flow fluctuations, and by properly calibrating the geometry of this chamber in relation to the duct's dimension and wave's frequency, it is possible to obtain effective acoustic damping because of the viscous dissipation induced by the velocity gradients which occur inside the chamber, a behavior similar to the mass-spring-dumper model excited by a force which absorbs kinetic energy.

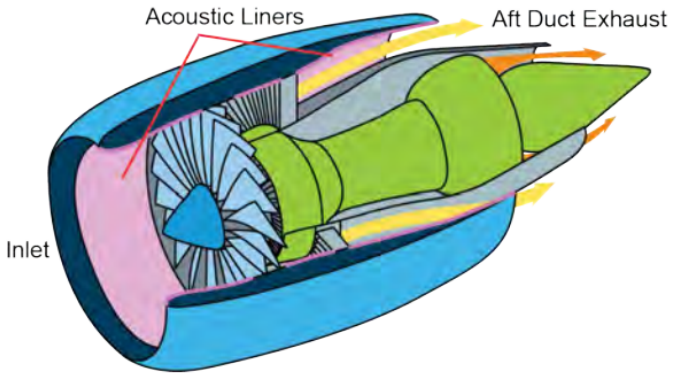

Fig. 2.1 A sketch of an aeronautical turbofan engine with acoustic liners installed on the inlet and aft duct exhaust walls [24].

This setup results in an acoustic discontinuity that generates a reflected wave and attenuates the transmitted one [1]. A proper dimensioning and combining of different layouts permits us to concentrate the dissipation on a single or multiple bandwidths. The single degree-of-freedom (SDOF Figure 2.2-a) design, consists of honeycomb cavities between a rigid backplate and a perforated sheet facing the flow containing acoustic energy, which are disposed in the stream from ducts and walls, are effective within a narrow frequency range, approximately one octave, and need to be designed *ad hoc* to the frequency band of primary concern for suppression, such as fan tone. The double degree-of-freedom (DDOF Figure 2.2-b) design is obtained by adding another layer with a porous septum inside the cavity, analogous to stacking two SDOF sandwiches with possible different cavities' geometry. With careful design, the DDOF setup can cover the frequency of major concern, for example, the *blade passing frequency* (BPF), and its next two harmonics, providing a useful bandwidth of attenuation of about two octaves, which is typically sufficient for turbofan engine applications. This concept can also be extended to multiple stacked layers and proper bandwidths. There are more designs with their peculiarities that rely on the same principle, e.g. the bulk absorber, which allows suppression in the widest bandwidth, but its use in civil aviation is limited because of installation and construction issues.

In aeronautical applications, the common objective is reducing emissions of specific sources (not only acoustically speaking), and both SDOF and DDOF liners, with their perforated face sheets, allow for absorption that is spatially concentrated; in fact, they are referred to as *local-reacting*, in opposition to *extended-reacting* liners, which can be thought like a layer of foam without the partitioning of the various chambers, and possessing less resonant behavior, they effectively absorb a broad range of frequencies, but result impractical for aeronautical applications. Hence, the local-reacting liners produce a greater dumping over a narrow frequency bandwidth matched to the noise sources of main concern; these, in fact, act like arrays of the previously mentioned Helmholtz resonators, and with proper distancing of orifices from each other, their mutual interaction can be

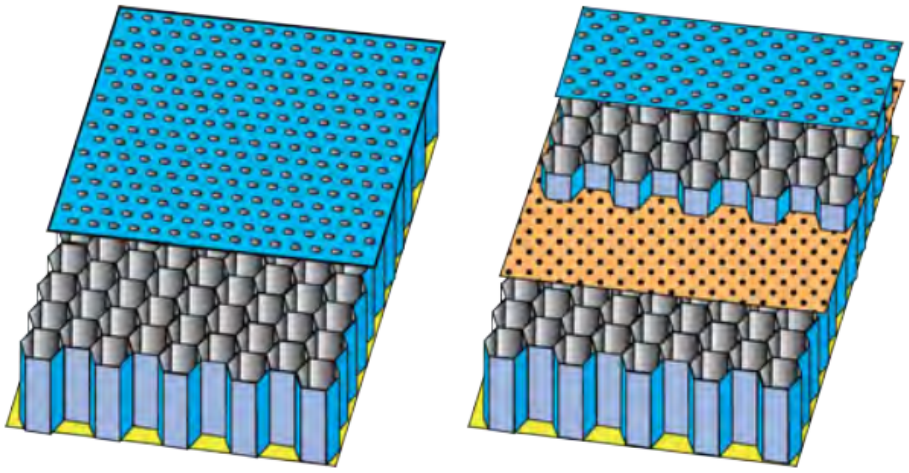

(a) SDOF (b) DDOF

Fig. 2.2 An example of SDOF design (a) and DDOF design (b). The geometry of cavities can change through a single layout and between different layouts(in case of multiple DOFs) [24]

neglected and account for the whole array's contribution. In this way, the microfluid flow field of a resonator perturbed by an incident or grazing wave can be analyzed independently.

2.1.2 Liners' design

Acoustic impedance, Z, is used to measure the opposition of a system to acoustic flow and is defined as the ratio of acoustic pressure p to velocity $\mathbf{v}$ measured on a surface perpendicular to the defined direction $\mathbf{n}$ (Equation 2.1). Both pressure and velocity are complex coefficients and functions of frequency ω, therefore, the result is a complex number, the real part of which is named resistance R, and the imaginary part X, reactance. It can characterize the behavior of acoustic liners and, in particular, help to determine how well the absorption of acoustic energy will occur under particular flow conditions [1].

$$\hat{Z}_n(\omega) = \frac{\hat{p}(\omega)}{\hat{\mathbf{v}}(\omega)\cdot\mathbf{n}} = R + iX \tag{2.1}$$

Acoustic impedance can be normalized by the characteristic impedance of air (or medium, in general), ρc, where ρ is the density of air and c the speed of sound propagation, both under reference conditions. Thus, it is possible to express the specific acoustic impedance with ζ and with θ and χ the real and imaginary parts, respectively [1].

$$\frac{\hat{Z}_n}{\rho c} = \zeta = \theta + i\chi \tag{2.2}$$

The general formula for a single degree-of-freedom acoustic liner can be expressed as follows.

$$\frac{\hat{Z}}{\rho c} = \zeta = \theta_m + i\Big(\chi_m + \chi_c\Big) \tag{2.3}$$

accounting for the resistance and reactance of the face sheet, θ_m and χ_m, respectively, and χ_c the cavity reactance which can be approximated to $-\cot(kh)$ (wave number k, cavity depth h). To better understand the roles and functioning of acoustic liners, it is possible to introduce an analogy to a mass spring-damper model (MSD) [32], Equation 2.4.

$$m\ddot{\mathbf{x}} + c\dot{\mathbf{x}} + k\mathbf{x} = \mathbf{F}_{ext} \tag{2.4}$$

By assuming an oscillating velocity, $\dot{\mathbf{x}} = |\dot{\mathbf{x}}|e^{i\omega t}$, it is possible to express the impedance of the mass-spring-damper system as the force-to-velocity ratio and intuitively relate it to the acoustic impedance.

$$Z(\omega) = \frac{\mathbf{F}}{\dot{\mathbf{x}}} = c + i\Big(\omega m - \frac{k}{\omega}\Big) \tag{2.5}$$

Where $\mathbf{F}$ is intended as the sum of the reaction forces of the mass, the spring and the damper; comparing the Equation 2.5 with 2.2, in terms of aeroacoustic analogy, it is evident that resistance θ is conceptually the damping term c, accounting for viscous dissipation and vortex shedding, while the reactance χ is a combination of mass inertia and elastic term, assigned to fluid inertia and compressibility [32].

The impedance presented to a sound wave that travels along the liners' surface depends upon the direction in which it is measured, frequency, and environment of the incident wave. The fraction of incident energy absorbed by the surface is denoted by α, with ϕ the angle of incidence ($\phi = 0°$ for the perpendicular incidence of a wave on a surface), and the following formula expresses this for the idealized case of an incident plane wave on a flat surface [36].

$$\alpha = \frac{4\theta\cos\phi}{(1+\theta\cos\phi)^2 + (\chi\cos\phi)^2} \tag{2.6}$$

Consequently, results that both the impedance of an acoustic liner, and the corresponding sound absorption, are frequency dependent; thou the Equation 2.6 is invalid in the case of waves propagating along a surface (parallel to it). The duct geometry directly affects sound absorption, while the impedance is an intrinsic property of an acoustic liner, and

being independent of duct geometry, its use results more appropriate in the liners' design process, where a controlled environment can be used to determine its acoustic impedance and consequently indicate the final sound power absorption occurring in the end product, e.g., aircraft engine nacelle. Since the last considerations, it is possible to associate the acoustic resistance θ as a measure of the forces responsible for the dissipation of the acoustic energy, while the reactance χ is related to the phase relationship between pressure and velocity, accounting only for hydrodynamic fluctuations but without possessing an acoustically relevant energy content, as arises in case the phases do not match [1].

In order to describe the acoustic properties of liners, an appropriate model for acoustic impedance has to be adopted and the most popular of semi-empirical models is the one developed by Guess [16], which derives the expressions for non-dimensional resistance $\theta(\omega)$ and reactance $\chi(\omega)$, as functions of geometrical and design parameters, there are available more specific and advanced impedance models for accurately predicting new experimental data of a particular setup.

$$\theta(\omega) = \frac{\sqrt{8\nu\omega\tau^*}}{\sigma c d} + \frac{\pi^2}{2\sigma}\left(\frac{d}{\lambda}\right)^2 + \frac{(1-\sigma^2)}{\sigma}\cdot\frac{|\tilde{\mathbf{v}}_{or}| + |\mathbf{u}'|}{c} \tag{2.7}$$

$$\chi(\omega) = \left(\frac{\omega\tau}{\sigma c} + \frac{\sqrt{8\nu\omega\tau^*}}{\sigma c d}\right) + \frac{\omega\delta}{\sigma c} - \cot\left(\frac{\omega L}{c}\right) \tag{2.8}$$

Where ν is the cinematic viscosity, σ the surface porosity, d the diameter of the orifice, τ the thickness of the plate, and λ the acoustic wavelength. In addiction, this model attempts to account for non-linear effects on resistance due to orifice velocity magnitude $\tilde{v}_{or}$ and using the magnitude of tangential velocity fluctuations u' to account for the mean flow effect. The end correction τ^* represents the small mass of air driven to the exterior of the holes due to the elastic behavior of fluid within the cavity, and δ is the term 'end correction' of the orifice. Although several studies [23] were conducted to validate the behavior of the model, there was evidence of some difficulties in predicting new experimental data and highlighting the dominant effect of grazing flow on acoustic resistance.

By defining p' the variation of pressure in respect to the reference pressure, and p'_{rms} its root-mean-squared value which is, in case of a signal with period T,

$$p'^2_{rms} = \frac{1}{T}\int_{t_0-T/2}^{t_0+T/2} p'^2(t)dt \tag{2.9}$$

Sound pressure level (SPL) is a measure of the intensity of sound, it measures the pressure of an acoustic wave in reference to a defined pressure level, as it relates signals

variating on different orders of magnitude, it results appropriate to express it in decibels (dB).

$$SPL = 10\text{Log}\left(\frac{p'^2_{rms}}{p^2_{ref}}\right) = 20\text{Log}\left(\frac{p'_{rms}}{p_{ref}}\right) \tag{2.10}$$

If air is considered, it is common to use the threshold of human audibility as the reference pressure $p_{ref} = 20\mu Pa$.

2.1.3 Non-linear behaviours

Sound pressure level dependency: SPL plays an important role in determining the response of acoustic liners, which can behave linearly or non-linearly [32]. In fact, a very complicated and not fully understood behavior is observed when acoustic liners are exposed to pressure waves above a certain SPL, the liners' response passes from being linear to nonlinear.

At SPL lower than 130 dB and at low Mach numbers, the linear response of the liners consists of laminar flow at the entrance of the resonance cavity and up to 60% of acoustic energy being depleted through viscous dissipation[51], Figure 2.3a. But, for SPL greater than 140 dB, intense vortex shedding occurs in the region of the orifice, internally and externally. The shedding mechanism involves the formation of counter-rotating vortices pairs, and it is of particular interest because in these conditions the sound absorption mechanism is about 12.5 times more efficient than in the case of simple viscous damping [51], Figure 2.3b, in order to observe this particular non-linear behavior, it results necessary to set up a particular frequency threshold, as the phenomenon results also frequency dependent [38].

The Grazing Flow's effect: is referred to the presence of a mean flow in the duct, resulting in a vortex sheet formed in the upstream corner of a hole. This induces an interaction between the acoustically induced flow and the duct's grazing flow, followed by a partial transfer of the acoustic energy from the incoming waves towards the vortex sheet, affecting broader frequency bands than in no-flow condition [55]. At higher Mach numbers, interaction between the upstream and the downstream vortices occurs, resulting in a more complex flow field, and even more interactions occur in the presence of turbulence. Furthermore, this vortex street is swept downstream, interfering with regular flow and also reducing the effective area useful for flow into the cavity [51].

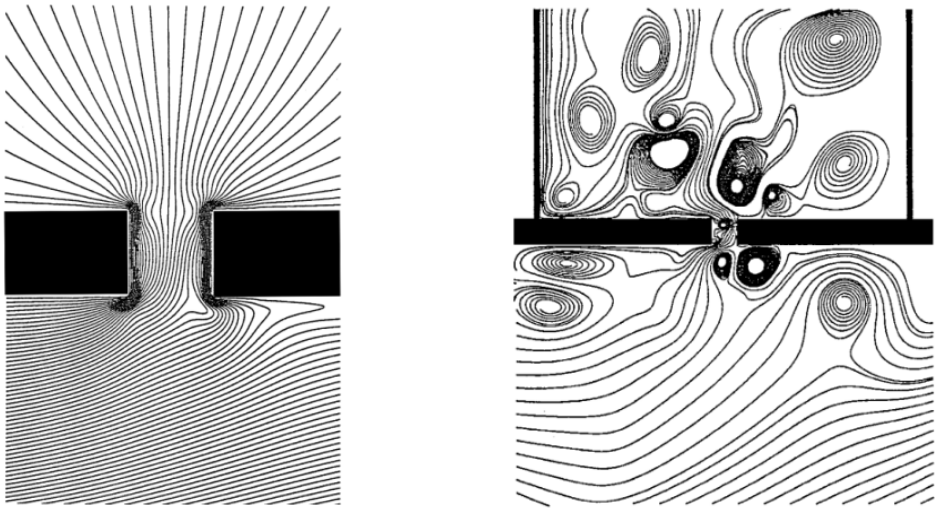

(a) linear (b) non-linear

Fig. 2.3 a) Instantaneous streamline pattern at the neck (orifice) of the resonator SPL=120 dB, f=3 kHz; b) Instantaneous streamline patter showing the shedding of vortices inside and outside the resonator at SPL=150 dB, f=3 kHz [51].

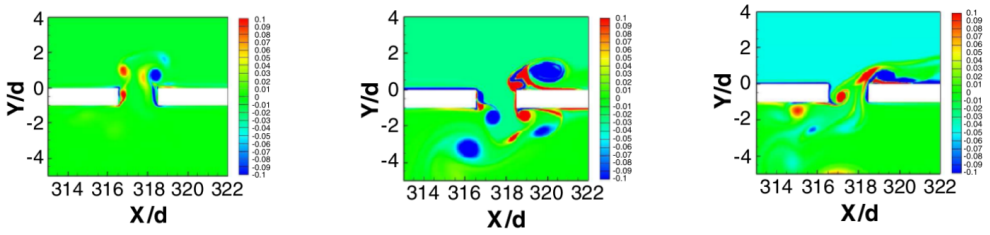

Fig. 2.4 Instantaneous vorticity contours near orifice wall in presence of grazing flow for three different Mach numbers, e.g. M={0.15, 0.5, 0.85} f=500 Hz.

Drag increase: Turbulent flow sees the presence of liners, in particular orifices that define the permeable surface, such as roughness, characterized by geometrical factors such as orifice size, shape, and their distribution (porosity) on the surface. The interaction occurs between the drag-produced and the sound-induced pressure gradients, resulting in an increase in wall shear stress together with a thickening of the boundary layer before entry into the cavity. As an additional effect, the presence of liners influences the overlaying turbulent stream, decreasing the streamwise velocity fluctuations [22]. Recent studies were directed to establish a relationship between relative drag contributions as a function of SPL [55], and apparently the liner-induced drag is also likely a function of sound amplitude also, Figure 2.5. As the decibels increase, the relative drag contributions of the face sheet and the orifice tend to be comparable. In general, the installation of the liners results in a large increase in drag (up to 70%, depending on the particular geometry and porosity) compared to a smooth wall.

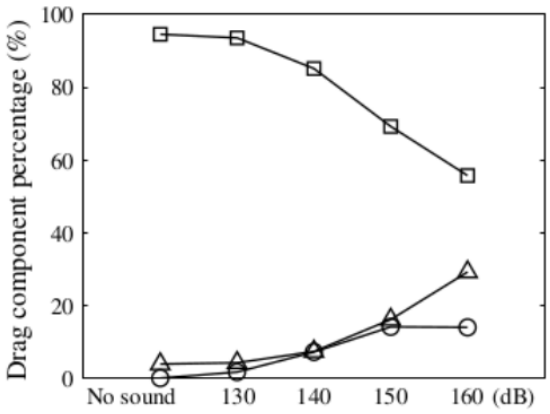

Fig. 2.5 Relative contributions of the face sheet (squares), cavity (circles), and orifice walls (triangles) to drag for different SPL at f=3 kHz.

2.2 Modal Decomposition

Lumley introduced Proper Orthogonal Decomposition (POD) for statistically stationary flows (flow fields whose mean and variance do not change over time) [34, 30], it is known by names like principal component analysis (PCA), Karhunen–Loève decomposition and many other denominations depending on the field of application. Currently, classical POD is one of the most adopted techniques for extracting structures based on their spatial coherence from time-dependent flow field data, POD seeks a set of deterministic modes that optimally capture the energy, or variance, of an ensemble of stochastic flow data, these modes do not necessarily evolve coherently in time, and **the part of the flow described by a particular space-only POD mode is not necessarily correlated with the part of the flow described by the same mode at a later time**, nor it is necessarily uncorrelated with the part of the flow described by a different mode at a later time. Once a proper inner product has been defined, it is possible to represent the total or a defined fraction of the energy of the flow field by the sum of the eigenvalues corresponding to the extracted modes, since each of them gives the average energy captured by its respective mode. Consequently, classic POD modes optimally represent spatial correlations within the flow.

The Spectral POD (SPOD)[4] is a particular form of classic POD and is not itself a recent achievement. Introduced by Picard & Delville [39] and based on the early work of Lumley [34] in 1970, it involves the decomposition of the cross-spectral density (CSD) tensor and leads to **orthonormal modes that represent physically meaningful coherent structures in the sense that each mode evolves coherently in space and time and the part of the**

[4] A homonymously named technique was introduced by Sieber *et al.* [47], Spectral Proper Orthogonal Decomposition, which improves and smoothens the information obtained from classical POD using a Discrete Fourier Transform (DFT) and by filtering the temporal correlation matrix, which represents the spectral content of the coherent structures captured. Describing this different technique can be misleading, so further details are omitted.

flow described by a particular SPOD mode is perfectly correlated with the part of the flow described by that same mode at all times and entirely uncorrelated with the part of the flow described by all other modes at all times; in this sense, with an appropriate inner product, it is possible to represent a certain fraction of energy of the flow field not only relying on spatial coherence but also focussing on particular frequency at all times [53].

The main difference between the two techniques, Spectral POD and Classic POD, stems from the definition of their source of information; the first uses time-dependent flow data keeping the evolution and the correlation of certain structures, and thus retains its dynamical information, while the second considers each snapshot as an independent realization of a random process discarding temporal evolution of the flow.

In a recent study [28], proper orthogonal decomposition was used to detect the most energy-containing structures to be used as base functions in the reduced-order model [6]. In a reduced-order model, perturbations from steady state are approximated by a linear combination of the eigenmodes. The dynamics of the flow field was decomposed into its global modes[5], and a reduced order model, consisting of only the most dominant modes, was used as source data. Demonstrating the strength of the method used and the ability to identify sound-generating structures. The flow field eigenmode decomposition was applied to a low-Mach number flow over a long, shallow cavity with smoothed corners, and the sound generated by the individual global modes was calculated. From the decomposition, it was concluded that the most sound-generating modes were governed by the collision of convecting instabilities in the shear layer and disturbances in the recirculation zone, as they impinged on the downstream edge of the cavity [28].

Despite their differences and those of other techniques, previously mentioned and omitted, the common objective is to decompose a complex phenomenon into a series of simpler components, or *modes*, defined in a certain domain in which coherence is requested, and possibly assign to each of them a specific role in the global picture. Once decomposed, the initial problem can be reformulated using a *reduced-order model* by keeping the principal components (dominant modes) which effectively account for the most energetically meaningful structures or mechanisms observed, or can be analyzed one piece at a time, as is usually desired for most complex cases. In the following figure (2.6) a simple example is presented: The reported diagram shows a complex non-linear flow field, resulting from two-dimensional laminar separated flow over a flat-plate wing, captured by a time series of instantaneous snapshots, by applying space-only POD first and then using only the mean flow field and the first two POD modes; it is possible to accurately represent the Von Kármán vortex street in the wake. By including additional (less energetically meaningful) modes (and structures), it is possible to reconstruct the original flow field

[5]Global modes are eigenmodes to the Navier–Stokes equations, linearized about a steady base flow [28].

more accurately, but with only minor changes with respect to the previous result. One more interesting aspect is that the dominant modes obtained and reported in Figure 2.6 are almost identical to those obtained from a different experiment [25] investigating a NACA 0012 airfoil in a three-dimensional turbulent flow.

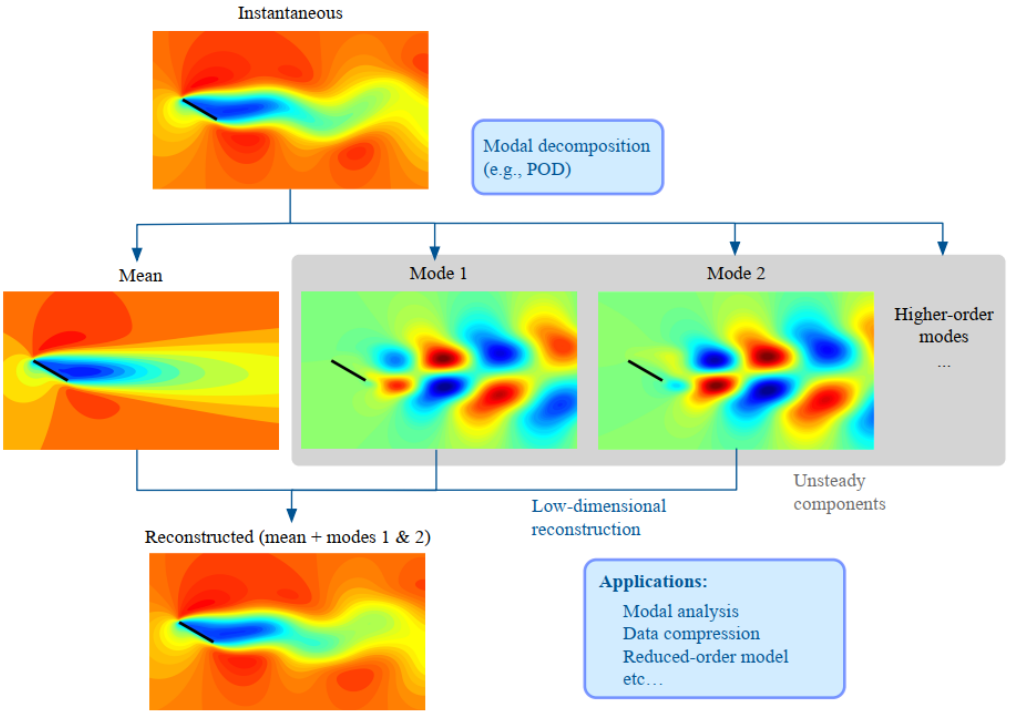

Fig. 2.6 Modal decomposition of two-dimensional incompressible flow over a flat-plate wing [7, 49] (Re = 100 and α= 30°). Visualized are the streamwise velocity profiles.

In order to properly approach the SPOD definition, use, algorithm, and comparison with other data-based techniques, some fundamental tools and concepts will be presented first.

2.2.1 SVD

Modal decomposition is an essential tool in every field from finance to facial recognition, to medical profiling, to fluid dynamics, and in anything else involving large data to be analyzed, and its foundation is *singular value decomposition* (SVD), which has many uses and interpretations, in order to determine the singular values (generalized eigenvalues) of matrix formatted data, detecting in this way the main elements, or patterns, or specifically modes of the entered data; once calculated, the *eigenmodes* can reveal certain physics underlying the observed phenomena, making it possible the use of SVD to obtain optimal low-rank matrix approximations to reconstruct a reduced order model: just like in the previous example (Figure 2.6, where complex flow condition was modelled using only the first two dominant modes), data variables and entries can greatly outnumber the details

necessity or capability of the final application, **it can also be demonstrated that very high order modes can be associated with signal noise** [50].

The decomposition of eigenvalues is performed on square matrices, whereas the singular value decomposition is of a more general understanding, its *singular values* can measure the distance of a decomposed matrix from the set of singular matrices and can be performed on rectangular matrices also. The data of the flow fields can be compiled in vector form captured in different snapshots and dynamically stored in rows (or eventually columns), resulting in a rectangular matrix $A \in \mathbb{C}^{m\times n}$ with generally $m \neq n$. In matrix form, the key relationship can be expressed as

$$\mathbf{AV} = \mathbf{U\Sigma}$$

where $\mathbf{U} = [\mathbf{u_1 u_2} \cdots \mathbf{u_m}] \in \mathbb{C}^{m\times m}$ and $\mathbf{V} = [\mathbf{v_1 v_2} \cdots \mathbf{v_n}] \in \mathbb{C}^{n\times n}$ are unitary matrices of left and right singular vectors (columns), respectively [6]. $\Sigma \in \mathbb{R}^{m\times n}$ is the matrix of singular values of **A**, with hierarchically ordered elements $[\sigma_1 \geq \sigma_2 \geq \sigma_3 \cdots \geq \sigma_p \geq 0]$, and $p = \min(m,n)$. To isolate **A**, we multiply $\mathbf{V}^{-1}$=$\mathbf{V}^*$ from the right side, obtaining the canonical form:

$$\mathbf{A} = \mathbf{U\Sigma V}^* \tag{2.11}$$

Figure 2.7 gives a visual and intuitive understanding of the dimensions of the respective matrices involved, assuming *m*>*n*.

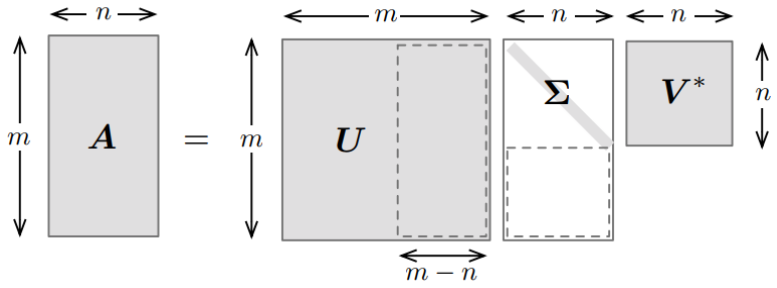

Fig. 2.7 SVD graphical decomposition with **A** *m-by-n* matrix [50].

It becomes instantly clear that once the product on the right-hand side occurs, some elements are lost due to multiplication by zeros (dashed rectangular areas in the Figure 2.7) so they can be omitted to save storage and the decomposition is denominated as *reduced* or *economy-sized SVD*. Therefore, the *reduced*-Σ ($\tilde{\Sigma}$) becomes a diagonal matrix of singular values.

[6] Unitary matrices **U** and **V** satisfy, $\mathbf{U}^*$=$\mathbf{U}^{-1}$, $\mathbf{V}^*$=$\mathbf{V}^{-1}$, with * denoting conjugate transpose.

As SVD is applied to a rectangular matrix, it is necessary to have two sets of basis vectors to define the domain and range of the matrix: the right singular vectors **V** that span the domain of **A** and the left singular vectors **U** that span the range of **A**, as illustrated in Figure 2.7. This is different from the eigenvalue decomposition of a square matrix, in which case the domain and the range are (generally) the same. While the eigenvalue decomposition requires the square matrix to be diagonalizable, SVD, on the other hand, can be performed on any rectangular matrix, making this last condition evident.

One of the resulting properties of the decomposition (also the most appreciated) is that the initial information contained in **A** is transferred and ordered hierarchically in $[\mathbf{U}, \Sigma, \mathbf{V}]$. That is, by selecting only a part of the singular values, it is possible to obtain a good approximation of **A**. The most common example of an application of SVD is digital images compression, the most part of the information is stored in only a fraction of the beginning storage size. In the Figure 2.8, it is possible to observe the portion of total information (energy) energy captured by the first **r** eigenvalues resulting from the SVD decomposition, version b) reproduces most of the details of the original picture, c) reliably reproduces most of the main features, while version d) despite it necessitates only 1.67% of the original's storage, is sufficient just for a basic understanding of the subject.

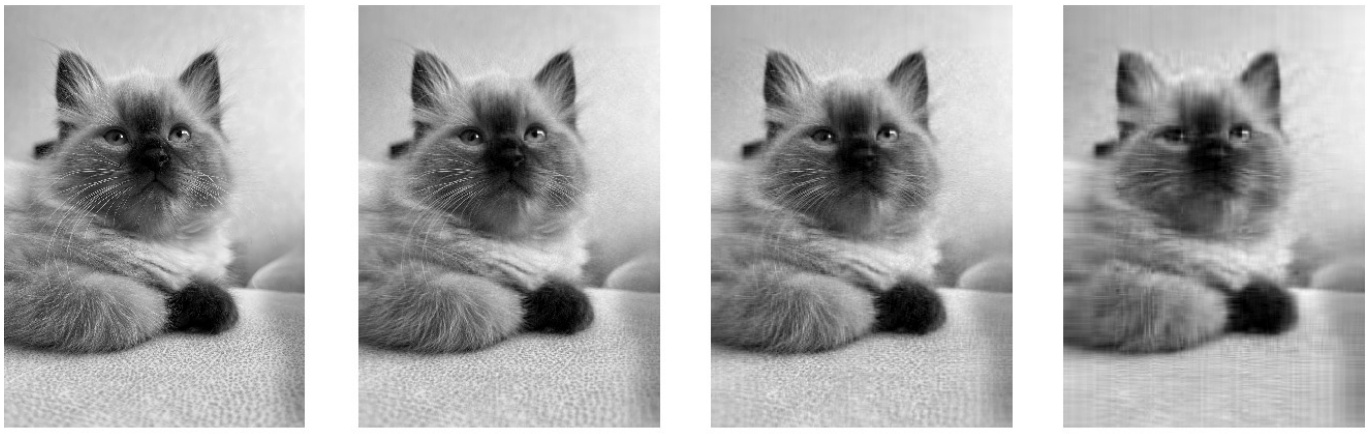

a) Original image. b) First 100 eigenvalues, 70.51% information, 8.55% size. c) First 50 eigenvalues, 61.64% information, 4.17% size. d) First 20 eigenvalues, 53.68% information, 1.67% size.

Fig. 2.8 Example of image compression obtained by using SVD.

2.2.2 PCA

Principal Component Analysis (PCA) is one of the central uses of the SVD, providing a coordinate system to represent highly dimensional correlated data. The key operation executed is the subtraction of the mean value and normalizing the variance before performing the SVD, the proper inner product will determine the orthogonality properties, so the

principal components will result uncorrelated (orthogonal) with each other, but will have maximal correlation with the measurements [13, 19, 3].

Typically, a number of measurements are collected in a single experiment, and these measurements are arranged into a row vector. A measurement may be the pressure registered in nodes of a grid from an instantaneous flow fields recording. A number of experiments are conducted, and each measurement vector is arranged as a row in a large matrix **A**, individual features *snapshots* are arranged as columns.

Recording data from n different experiments (e.g. instantaneous pictures) for m measurements (probes available in a domain), a matrix **A** (n-*by*-m) is obtained. Subtracting the mean value, $\overline{\mathbf{A}}$ from **A** itself, results in the mean-subtracted data **B**, and its covariance matrix **C**:

$$\mathbf{B} = \mathbf{A} - \overline{\mathbf{A}}$$

$$\mathbf{C} = \frac{1}{n-1}\mathbf{B}^{*}\mathbf{B}$$

$$\mathbf{CV} = \mathbf{VD} \tag{2.12}$$

The first principal component $\mathbf{u_1}$ will be the eigenvector of $\mathbf{B}^{*}\mathbf{B}$ corresponding to the maximum magnitude eigenvalue; consequently, it becomes obvious that u_1 is the left singular vector of **B** corresponding to the largest singular value. The principal components are computed by the eigendecomposition of C, with matrix **V** resulting the equivalent of **V** during SVD.

2.3 Classic POD

2.3.1 Generalities

Classic POD (and all of its alternative denominations previously presented), since now space-only POD or simply POD, has its roots in SVD and is a modal decomposition practice for extracting modes from a set of data, more precisely and general from *any* matrix, providing the algorithm to obtain minimal number of basis functions or modes ϕ that, on average, best approximate a zero-mean stochastic process, based on a finite ensemble of samples, permitting also to set a threshold for desired approximation accuracy, or energy fraction to keep, relying on optimizing the mean square of the field variable being examined.

The starting point, similarly to PCA, is subtracting the temporal mean value from the examined field variable (e.g. velocity):

$$\mathbf{q}'(\xi,t) = \mathbf{q}(\xi,t) - \overline{\mathbf{q}}(\xi)$$

with ξ spatial coordinate vector and by defining $\phi_j(\xi)$ spatial modes and $a_j(t)$ time-dependent expansion coefficients; stems the following decomposition[7]:

$$\mathbf{q}'(\xi,t) = \sum_j a_j(t)\phi_j(\xi) \tag{2.13}$$

representing the flow field on the basis of a series, analogously to a generalized Fourier series with set of functions ϕ_j. By defining the stochastic ensemble to consist of snapshots of the flow field in different time instances, the flow is treated as instantaneous realizations of a stochastic process. In the framework of POD, we seek the optimal set of basis functions for a given flow field data.

There are numerous different variations of POD, indeed it is one of the most used and simplest techniques in post-processing and analysis in fluid dynamics, based on coherent's structures domain of interest for every kind of applications, among which fundamental analysis of fluid flows, aerodynamic design optimization and flow control, reduced order modelling, etc.

As inputs for the POD, it is possible to use snapshots of any scalar or vector field (pressure, temperature, velocity, vorticity, etc.) regardless of the dimensional extension (dimension of ξ) over discrete times t_i. And the outputs are a set of modes $\phi_j(\xi)$, orthogonal according to a defined inner product, with their corresponding temporal coefficients $a_j(t)$, and energy levels λ_j, hierarchically ordered. The fluctuations in the original field are expressed as a linear combination of the modes and their corresponding temporal coefficients according to the equation. 2.13.

2.3.2 Procedure for space-only POD

Reporting for simplicity the formulation of Equation 2.13, we define $\mathbf{x}(\xi,t)$ as the fluctuating part of the vector.

$$\mathbf{x}(\xi,t) \equiv \mathbf{q}'(\xi,t) = \sum_j a_j(t)\phi_j(\xi) \tag{2.14}$$

[7]Note that Equation 2.13 explicitly employs a separation of variables, which may not be appropriate for all problems; alternatively, a fallback to the original version of POD is possible, where a_j are only expansion coefficients and $\phi(\xi,t)$ are the spatio-temporal modes [18].

The objective is to find vectors $\phi_j(\xi)$ to represent $\mathbf{q}(\xi)$ with the least number of elements (modes).

$$\mathbf{q}(\xi,t)-\overline{\mathbf{q}}(\xi)=\mathbf{x}(\xi,t)\in\mathbb{R}^n, \qquad t=t_1,t_2,\ldots,t_m$$

$$\mathbf{X}=[\mathbf{x}(t_1),\mathbf{x}(t_2),\ldots,\mathbf{x}(t_m)]\in\mathbb{R}^{n\times m} \tag{2.15}$$

$$\mathbf{R}=(1/m)\mathbf{X}\mathbf{X}^T=\sum_{i=1}^{m}\mathbf{x}(t_i)\mathbf{x}^T(t_i)\in\mathbb{R}^{n\times n} \tag{2.16}$$

In Equation 2.15 we have introduced the matrix $\mathbf{X}$ representing all available data, that is, m-snapshots of a domain long n-points, and also the spatial dependence was reduced to emphasize the time dependence of the snapshots ($\mathbf{x}(\xi,t)\Rightarrow\mathbf{x}(t)$), and in Equation 2.16 its covariance matrix $\mathbf{R}$. Now we have the solution to Equation 2.14 that can be formulated using the eigendecomposition.

$$\mathbf{R}\phi_j=\lambda\phi_j, \qquad \lambda_1\geq\lambda_2\geq\ldots\geq\lambda_n\geq 0 \tag{2.17}$$

The eigenvectors obtained this way are the orthogonal POD modes, having their inner product[8] to meet the condition

$$\langle\phi_j,\phi_k\rangle\equiv\int_V\phi_j\cdot\phi_k dV=\delta_{jk}, \qquad j,k=1,\ldots,n.$$

In case the velocity vector is used in $\mathbf{x}(t)$, the eigenvalues λ_j will account for the kinetic energy captured by a single mode ϕ_j, ordered in terms of energetic importance (magnitude); using a vorticity field will produce the entropy content. Analogously to the SVD, by keeping only a set of first $\mathbf{r}$ modes (truncating the series) will limit the level of energy captured by the selected modes, and the smallest scales will be ignored in favor of the greatest, dynamically important, structures representing the dominant phenomenon of the flow (e.g. vortex shedding, Kelvin-Helmholtz instability, etc.). Analogously to the previous example of the use of SVD (Figure 2.8), where instead of the energy captured by coherent structures representing the main features of the phenomenon, different amounts of pixels were used to represent the details of the cat, the relative energy (instead of conserved

[8] In general, where a non-uniform grid is used, the volume integral (inner product) should include the cells weights $\mathbf{W}$ for each data point. Consequently, the covariance matrix will be formulated as $\mathbf{R}\equiv(1/m)\mathbf{X}\mathbf{X}^T\mathbf{W}$, with $\mathbf{W}$ the defined spatial weights.

information) f captured by the first $\mathbf{r}$ modes over a total of n modes, can be expressed by

$$\mathrm{f} = \sum_{j=1}^{r} \lambda_j / \sum_{j=1}^{n} \lambda_j.$$

The temporal coefficients $a_j(t)$, generally contain a mix of frequencies, and this aspect will be compared with respect to spectral POD.

$$a_j(t) = \langle \mathbf{q}(\xi,t) - \overline{\mathbf{q}}(\xi), \phi_j(\xi) \rangle = \langle \mathbf{x}(t), \phi_j(\xi) \rangle$$

The presented procedure to perform the POD is the classic one, but there are several others that obtain the same result in a more efficient way [50], such as the method *of snapshots* or simply by using *SDV*.

Reduced-order modelling: Thanks to their orthogonality property, POD modes ca, and have been used to obtain reduced-order models for various flow conditions [37, 43]. In addition, the Galerkin projection method can be used to reduce the high-dimensional discretization of partial differential equations into reduced-order ordinary differential equation models for temporal coefficients $a_j(t)$ [50].

Outlook: Space-only POD, is a simple yet powerful method that produces an orthogonal set of basis vectors with minimal dimension (this property is useful in constructing a reduced-order model of the flow field). The resulting modes are arranged by their energy content but not by dynamical importance, and hence it is unclear how many modes are relevant for a reliable model not to lose some of the small-scale yet dynamically important structures; from a different point of view, this feature can be useful to filter higher-order modes assuming them as incoherent noise data.

Example: the example represented in Figure 2.6 of the previous section is a perfect showcase of the Proper Orthogonal Decomposition potential; in fact, POD modes are commonly used to construct a reduced order model to study main features of the flow fields, extract characteristic behaviors, and observe analogies between different experiments.

2.4 Spectral POD

2.4.1 Generalities

In order to overcome some of the limitations imposed by space-only POD, we can seek modes that depend on both space and time instead of only space; just as it happens in every other field: once a phenomenon is observed, to reveal more of the underlying physics and mechanisms, it is very useful to inspect the same information in the frequency domain. Hence, by realizing temporal Fourier transforms of the flow field, power spectra can be obtained, and after a specific process, time-harmonic modes at discrete frequencies can be extracted; these form an orthogonal basis optimally ranked in terms of energy, defining the Spectral POD functionality. Since space-only POD reduces to harmonic analysis over directions that are stationary or periodic, SPOD is effective in extracting coherent structures from statistically stationary flows, where the mean flow field remains constant. One of the different requirements is that flow field data is composed of a set of realizations of the time-dependent flow, not just a stochastic set of snapshots, as happens with standard POD.

2.4.2 Method

When stationarity is an appropriate assumption, it can be exploited in different ways. By considering both spatial and temporal variables $\mathbf{x}_i(\xi,t)$, and defining the inner product as

$$\langle \mathbf{x}_1, \mathbf{x}_2 \rangle = \int_{-\infty}^{\infty} \int_{\Omega} \mathbf{x}_1^*(\xi,t) W(\xi,t) \mathbf{x}_2(\xi,t) d\xi dt \tag{2.18}$$

with a properly selected, positive-definite Hermitian matrix $W \in \mathbb{C}^{N \times N}$, which accounts for spatial weights and the numerical quadrature on the discrete grid, $W(\xi)$. In this way, it is possible to solve a series of POD problems in Fourier space, one frequency at a time. The cross-spectral density (CSD) tensor is the kernel of the eigenvalue problem to find a set of modes that result orthogonal under the whole space-time domain.

Once introduced the classic POD, there are only a few more steps to formulate its spectral version. Spectral POD can be estimated from a time series of snapshots in the form of $\mathbf{X}$ (Equation 2.15, reported hereafter for simplicity), moving to the frequency domain, using Welch's averaging method [54] to estimate the CSD tensor, and finally solving the SVD problem, or eventually the eigenvalue problem:

$$\mathbf{X} = [\mathbf{x}(t_1), \mathbf{x}(t_2), \ldots, \mathbf{x}(t_m)] \in \mathbb{R}^{N \times N_t}$$

1. Firstly, the whole time series is subdivided into a number of N_b blocks of significant temporal duration, long enough to allow overlapping, consisting of N_f snapshots each. Again, spatial dependence was dropped to emphasize frequency content, $\mathbf{x}(\xi,t) \Rightarrow \mathbf{x}(t)$, and denoting by l the l-th block

$$\mathbf{X}^{(l)} = [\mathbf{x}(t_1), \mathbf{x}(t_2), \ldots, \mathbf{x}(t_{\mathbf{N}_f})] \in \mathbb{R}^{N \times N_f}. \tag{2.19}$$

2. Under the ergodicity hypothesis, each block can be regarded as a statistically independent realization of the flow. Welch's periodogram averaging method is used by executing the Fourier transform of each block, obtaining data on the discrete frequency range:

$$\mathbf{X}^{(l)}(\xi,t) \quad \longrightarrow \quad \hat{\mathbf{X}}^{(l)}(\xi,\omega)$$

$$\hat{\mathbf{X}}^{(l)} = [\hat{\mathbf{x}}(\omega_1)^{(l)}, \hat{\mathbf{x}}(\omega_2)^{(l)}, \ldots, \hat{\mathbf{x}}(\omega_{N_f})^{(l)}] \in \mathbb{R}^{N \times N_f} \tag{2.20}$$

$$\hat{\mathbf{X}}^{(l)}(\xi,\omega) = \sum_j \hat{a}_j(\omega)\phi_j(\xi,\omega) \tag{2.21}$$

$$\hat{a}_j(\omega) = \langle \hat{\mathbf{X}}(\xi,\omega), \phi_j(\xi,\omega) \rangle_x \tag{2.22}$$

3. All realizations of the Fourier transform at a specific frequency ω_k are collected into a new data matrix $\hat{\mathbf{X}}_{\omega_k}$

$$\hat{\mathbf{X}}_{\omega_k} = [\hat{\mathbf{x}}(\omega_k)^{(1)}, \hat{\mathbf{x}}(\omega_k)^{(2)}, \ldots, \hat{\mathbf{x}}(\omega_k)^{(N_b)}] \tag{2.23}$$

$$\hat{\mathbf{X}}_{\omega_\mathbf{k}} \hat{\mathbf{X}}^{\mathbf{T}}_{\omega_\mathbf{k}} \phi_{\omega_{k,j}} = \lambda_{\omega_{k,j}} \phi_{\omega_{k,j}}, \qquad \phi_{\omega_{k,j}} \in \mathbb{R}^N, \qquad \lambda_{\omega_{k,1}} \geq \lambda_{\omega_{k,2}} \geq \ldots \geq \lambda_{\omega_{k,N_b}} \geq 0$$

The cross spectral density (CSD) matrix is obtained from the product $\hat{\mathbf{X}}_{\omega_\mathbf{k}} \hat{\mathbf{X}}^{\mathbf{T}}_{\omega_\mathbf{k}}$, and its eigenvalue decomposition produces the spectral modes $\phi_{\omega_{k,j}}$ (principal components) and $\lambda_{\omega_{k,j}}$ their respective modal energies. Furthermore, the resulting modes are orthogonal under the space-time inner product, so each mode at each frequency can be considered as a distinct mode, uncorrelated with all other modes. The spectral POD formulation leads to modes that oscillate, each at a single frequency, and optimally represent the second-order space-time flow statistics, representing coherently evolving structures, in space and time. In other words, the part of the flow described by a particular SPOD mode is perfectly correlated with the part of the flow described by that same mode at all times and entirely uncorrelated with the part of the flow described by all other modes at all times **SPOD**

modes decouple flow phenomena at different time scales, which can be helpful for understanding the flow dynamics and deriving non-empirical models [53].

2.4.3 Algorithm and key parameters

While various algorithms for space-only POD computing are available and widely adopted (including the previously described method)[9], the precise universally adopted algorithm for determining SPOD modes is still a poorly documented matter, a subject of research, and requires several additional considerations. In the following paragraphs, one of the most recent formulations of the procedure to calculate the spectral POD will be described, the one updated and reviewed by A.Towne, T.Schmidt, and T.Colonius [53]. It is worth specifying that the authors mentioned above have introduced a version of the SPOD specifically meant for situations where the data becomes too "large" for actual technology, named "streaming" SPOD (`sspod`) [46], computing decomposition on-the-go by saving storage and operating memory requirements, by updating the results dynamically and without limitations on the number of snapshots imported; as it calculates them one small batch at-a-time: as SPOD requires a large amount of data and information to analyze, higher spatial and time resolutions will give more information and details (one of the reasons why its adoption was unfeasible until recent times). Despite its flexibility in managing large data, only the main method will be described and adopted.

Using the previously introduced nomenclature, we denote by $\mathbf{x}_j \in \mathbb{R}^N$ the j^{th} instantaneous flow field data (snapshot) of a scalar or vector variable, e.g. pressure or velocity, $\mathbf{x}(\xi,t)$ in a discrete set of points ξ of spatial domain Ω at a specific time t_j. N is the length of the snapshot vector equal to the number of flow variables $q_i(\xi,t)$ times grid points:

$$\mathbf{x}_j = \mathbf{x}(\xi,t_j) = [q_1(\xi,t_j), q_2(\xi,t_j), q_3(\xi,t_j)] \qquad j = 1,2,\ldots,N$$

Considering M equidistant in time snapshots, the whole resulting flow field matrix $\mathbf{X}$ will be:

$$\mathbf{X} = [\mathbf{x_1}, \mathbf{x_2}, \ldots, \mathbf{x_M}] \in \mathbb{R}^{N\times M} \tag{2.24}$$

Increasing indefinitely M does not guarantee the convergence of the CSD estimates, as the uncertainty will result comparable to the estimate magnitude itself [14]. In order to obtain convergence, by the ergodicity hypothesis[10], it is necessary to increase the number of different experiments (with the appropriate averaging). A proven alternative

[9] One of the most adopted is based on the method of snapshots by Sirovich (1987) [48, 50]

[10] A sufficiently large collection of random samples from a process can represent the average statistical properties of the entire process.

solution is to use Welch's method [54], by using an improved periodogram spectrum estimation method (signal averaging of requested periods) reduces the noise by sacrificing the frequency resolution, in this way, it is also possible to estimate the uncertainty based on the length and noisiness of the data record [2]. The process is the same as that used to compute the power spectral density (PSD) of a single time series, but performed N_b times on subdivisions of the beginning data set.

The first step is to partition the time series of M snapshots, data matrix, into a set of smaller, overlapping N_b blocks composed of N_f snapshots each.

$$\mathbf{X}^{(l)} = [\mathbf{x}_1^{(l)}, \mathbf{x}_2^{(l)}, \ldots, \mathbf{x}_{N_f}^{(l)}] \in \mathbb{R}^{N \times N_f} \tag{2.25}$$

Denoting by N_{ov} the number of snapshots by which one block overlaps with the adjacent one, the total number of blocks will result[11]

$$N_b = \left\lfloor \frac{M - N_{ov}}{N_f - N_{ov}} \right\rfloor \tag{2.26}$$

The next step is to calculate the *Discrete Fourier Transform* (`DFT`) on each block of N_f snapshots, so the block l^{th} ($l = 1, \ldots, N_b$) will result in:

$$\hat{\mathbf{X}}^{(l)} = \texttt{DFT}(\mathbf{X}^{(l)})$$

$$\hat{\mathbf{X}}^{(l)} = [\hat{\mathbf{x}}_1^{(l)}, \hat{\mathbf{x}}_2^{(l)}, \ldots, \hat{\mathbf{x}}_{N_f}^{(l)}] \qquad l = 1, 2, \ldots, N_b \tag{2.27}$$

Once transformed, the data are represented at discrete frequencies $f_k = kN_f/T$, and if the original data are real-valued, then transformed data at negative frequencies in the above expression are redundant: they are conjugates of the corresponding positive frequencies and only positive frequencies need to be considered. However, the data are often complex, as is the case when the data have already been Fourier transformed in one or more homogeneous spatial directions. In this case, there is a subtlety. In the sampled data, the negative frequencies will not be redundant. However, the true (as opposed to sample) statistics of the positive and negative frequencies should be identical; for every POD mode of positive frequency, there should exist an identical one (with identical eigenvalue) for negative frequency. Therefore, it is advisable to average together positive/negative frequencies. The resolved frequencies will be:

[11] $\lfloor \cdot \rfloor$ denotes the floor operation.

$$f_k = \begin{cases} \dfrac{k-1}{N_f \Delta t} & \text{for} \quad k \leq N_f/2 \\ \dfrac{k-1-N_f}{N_f \Delta t} & \text{for} \quad k > N_f/2 \end{cases} \tag{2.28}$$

$\hat{\mathbf{x}}_k^{(l)}$ will contain the l^{th} realization (block) of the Fourier mode at the k^{th} discrete frequency f_k, and its inverse transform $\mathbf{x}_j^{(l)}$ will be respectively:

$$\hat{\mathbf{x}}_k^{(l)} = \sum_{j=1}^{N_f} \mathbf{x}_j^{(l)} e^{-i2\pi jk/N_f} \qquad k = -N_f/2, \ldots, N_f/2 \tag{2.29}$$

$$\mathbf{x}_j^{(l)} = \frac{1}{N_f} \sum_l \hat{\mathbf{x}}_k^{(l)} e^{i2\pi jk/N_f} \qquad j = 1, 2, \ldots, N_f \tag{2.30}$$

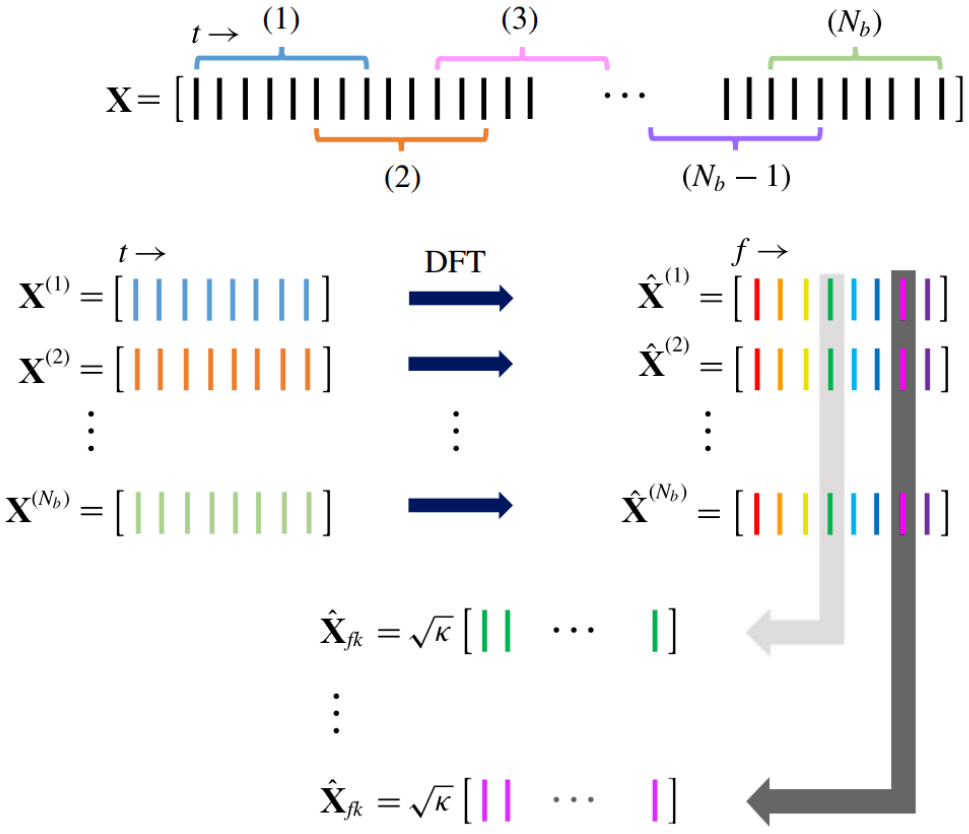

Fig. 2.9 A schematic representation of the snapshots' time series transform using DFT and overlapping: the whole time series is divided into overlapping N_b blocks (top) each block, on the left (represented by different colors) are then transformed in frequency domain on the right (each block has a discrete frequency set, multiple colors per each block). Finally, for each frequency, contributions are collected in $\mathbf{X}_{f_k}$ matrices, corresponding to the f_k frequency, with $\kappa = \Delta t/(sN_b)$. [53]

The cross-spectral density (CSD) tensor, $\mathbb{S}(\xi, \xi', f)$ for frequency f_k can be estimated by the average

$$\mathbb{S}_{f_k} = \frac{\Delta t}{sN_b} \sum_{l=1}^{N_b} \hat{\mathbf{x}}_l^{(l)} \hat{\mathbf{x}}_l^{*(l)} \qquad \text{with } s = \sum_{j=1}^{N_f} w_j^2 \tag{2.31}$$

By adopting a compact notation (Equation 2.32): assembling the matrix $\hat{\mathbf{X}}_{f_k}$ out of Fourier realizations from the columns corresponding to each k^{th} frequency of $\hat{\mathbf{X}}_{f_k}^{(l)}$ (noting that will result only one $\hat{\mathbf{X}}_{f_k}$ per frequency), the remaining analysis has to be performed one frequency at-a-time, and the following steps have to be repeated for each frequency.

$$\hat{\mathbf{X}}_{f_k} = \sqrt{\frac{\Delta t}{sN_b}} \cdot [\hat{\mathbf{x}}_k^{(1)}, \hat{\mathbf{x}}_k^{(2)}, \ldots, \hat{\mathbf{x}}_k^{(N_b)}] \in \mathbb{R}^{N \times N_b} \tag{2.32}$$

Consequently, the CSD tensor $\mathbb{S}$ for the frequency f_k can be expressed as

$$\mathbb{S}_{f_k} = \hat{\mathbf{X}}_{f_k} \hat{\mathbf{X}}_{f_k}^* \tag{2.33}$$

As stated, this CSD estimate converges as the number of blocks N_b increase, representing in this way a series of different experiments conducted in identical conditions [54, 2]. The number of snapshots N_f, determining the length of a single block, puts a limit on the frequency resolution of the final result, while the total number of snapshots $M \equiv N_T$, together with the number of overlapping frames N_{ov}, define the total number of blocks obtainable from a single data series long snapshots (both these aspects will be faced in the next paragraphs). Using this estimate, the infinite-dimensional SPOD singular value problem reduces to a $N \times N$ matrix eigenvalue problem at each frequency:

$$\mathbb{S}_{f_k} \mathbf{W} \Psi_{f_k} = \Psi_{f_k} \Lambda_{f_k} \tag{2.34}$$

The retrieved SPOD modes for the discrete frequency f_k, are the columns of Ψ_{f_k}, hierarchically ordered according to their corresponding modal energies (eigenvalues) stored in the diagonal matrix Λ_{f_k}. The obtained, approximate, modes mimic the properties of the continuous modes, e.g. orthogonality (Equation 2.35) and CSD tensor expansion (Equation 2.35):

$$\Psi_{f_k}^* \mathbf{W} \Psi_{f_k} = \mathbf{I} \tag{2.35}$$

$$\Psi_{f_k} \Lambda_{f_k} \Psi_{f_k}^* = \mathbb{S}_{f_k} \tag{2.36}$$

As the number of blocks N_b in reality happens to be much smaller than the discretized problem of size N, also the solution will be obtained from a matrix of size $N_b \times N_b$ instead of $N \times N$, hence the tilde sign in equations 2.37 and 2.38, defines the matrices and own elements obtained by facing a discretized problem instead of the theoretical one. By using the definition of $\mathbb{S}_{f_k}$ in Equation 2.33, it is possible to observe that the $N_b \times N_b$ eigenvalue problem in Equation 2.37, supports the same non-zero eigenvalues as the problem defined in Equation 2.34 with the corresponding eigenvectors in Equation 2.38.

$$\hat{\mathbf{X}}^*_{f_k} \mathbf{W} \hat{\mathbf{X}}_{f_k} \Theta_{f_k} = \Theta_{f_k} \tilde{\Lambda}_{f_k} \tag{2.37}$$

$$\tilde{\Psi}_{f_k} = \hat{\mathbf{X}}_{f_k} \Theta_{f_k} \tilde{\Lambda}^{-1/2}_{f_k} \tag{2.38}$$

2.4.4 Sampling Parameters

The accuracy of the estimation of modes and the respective modal energies depends on an accurate estimation of the CSD tensor $\mathbb{S}$ from time-dependent data, consequently the appropriate choice of parameters used to discretize (sample) the continuum (real) phenomenon is the key in obtaining the best approximation [2].

Weight Matrix: The proper weight matrix W choice, expressed during the continuous inner product computation (Equation 2.18), plays a role of great importance in SPOD analysis. It determines the optimality and orthogonality of the out coming modes, by representing the discrete quadrature of the inner product itself [45]. The weight matrix can also be used to apply SPOD to subdomains or a subset of the variables that comprise the solution vector, this can be done by assigning zero weight to the portions of the domain or variables that are to be excluded, alternatively, these parts can be removed from the data before computing the SPOD, this can be done by selecting determinate regions of interest (ROI)[12]. The most common choices of normalization for flow fields are the: *Variance, Weighted 2-Norm, Turbulence Kinetic Energy* and *Compressible Energy* norm.

Sampling frequency f_s: determines the number of snapshots obtained in 1 [s] or (conversely) the Δt between each of them; depends on the used instrumentation to acquire the measurements. f_s can be limited by the technological means or the desired timescale

[12]The advantage of retaining certain elements (grid nodes, cells or regions) with zero weight, is that they remain part of the spatially coherent SPOD modes, allowing their physical interpretation, but without changing the final spectrum [45].

dynamics to capture. Usually, a higher f_s is wanted because pre-processing techniques allow to reject unwanted information by filtering or averaging.

$$f_s = \frac{1}{\Delta t} \tag{2.39}$$

Moreover, the maximum resolvable (Nyquist) frequency, above which the signal at higher frequencies (if present in the data) introduces bias in the form of aliasing error, will be determined as

$$f_{\max} = \frac{f_s}{2} \tag{2.40}$$

Block size N_f: can be determined by the desired frequency resolution (bin size) Δf, that corresponds to the lowest resolvable frequency[13].

$$N_f = \frac{f_s}{\Delta f} \tag{2.41}$$

Hence, we can deduce that an accurate spectral estimation requires the highest possible f_s and N_f, such that sampling reproduces the true underlying spectrum best approximating the real phenomenon dynamics. However, by using Welch's method, all the data will come from a single time series long M snapshots, limiting the number of blocks to be created, especially when a large N_f is chosen. In order to achieve the convergence of the spectrum, an appropriate number of blocks has to be analyzed. A good practice to increase N_b, for statistically stationary flows, is overlapping the segments, shifting the starting point of a segment to 50% of the previous one, increasing this way their number. However, this number this can slightly differ to make use of all available snapshots.

2.5 Wavelet transforms method

2.5.1 Generalities

It is well known, that hydrodynamic pressure, being induced by the turbulent structures, is intrinsically intermittent, and this physical evidence motivated the use and improvement of the wavelet decomposition techniques rather than the Fourier transform for the analysis of vorticity and hydrodynamic pressure in turbulent flows. As the Fourier modes are not well suited to represent and describe intermittent events since they are localized in the spectral space but not in the physical one, the use of a wavelet basis results more

[13] That is not equal to zero. The close to zero frequency component itself is expected to be present if the block mean is close to the experiment's (true) mean.

advisable due to its **localization in both the physical and the transformed spaces.** With the purpose of analysing the near-field pressure, such an idea was exploited to develop a novel post-processing technique based on the application of wavelet transforms, as a procedure to separate the hydrodynamic from the acoustic pressures[15]; assuming that the hydrodynamic contribution related to localized eddy structures compresses well onto a wavelet basis so that it can be described by a few but with large amplitude wavelet coefficients. **Thus, the pseudo-sound can be extracted by selecting the wavelet coefficients exceeding a proper threshold. The acoustic counterpart associated with more homogeneous and low-energy fluctuations is represented by those coefficients having an amplitude lower than the threshold**. The advantage of this wavelet-based method with respect to previous approaches was mainly in the simplicity of the required set-up. Indeed, only two microphone signals in the near field, acquired (or computed) in two positions sufficiently close to each other, are needed to compute the cross-correlation between the presumed hydrodynamic and acoustic components. The computation of the cross-correlation was necessary to determine, through an iterative process, the amplitude of the threshold level.

Wavelet transforms are a recent mathematical technique, based on group theory and square integrable representations, which allows unfolding a signal, or a field, into both space and scale, and possibly directions, making use of analysing functions, called wavelets, which are localized in space. The scale decomposition is obtained by dilating or contracting the chosen analysing wavelet before convolving it with the signal. The limited spatial support of wavelets is important because then the behaviour of the signal at infinity does not play any role. Therefore, the wavelet analysis or synthesis can be performed locally on the signal, as opposed to the Fourier transform which is inherently non-local due to the space-filling nature of the trigonometric functions. Wavelet transforms have been applied mostly to signal processing, image coding, and numerical analysis, and they are still evolving [11].

By considering the presence of coherent structures in turbulent flows, which correspond to the condensations of the vorticity field into organized patterns, which contain most of the energy of the flow, and where non-linearity is reduced, or even cancelled when the coherent structures are axisymmetric; these coherent structures seem to play an important, but not yet well understood, dynamical role. And it may seem much more sense in decomposing a turbulent field into such localized oscillations of finite energy as wavelets, rather than into space-filling trigonometric functions which do not belong to the $L^2(\mathbf{R}^n)$ functional space and therefore are not of finite energy. Hence, as the continuous wavelet transform (CWT) offers a continuous and redundant unfolding, in terms of both space and scale, which may enable us to track the dynamics of coherent structures, and measure their contributions to the energy spectrum. In particular, the CWT is well suited for analysing the local differentiability of a function, and for detecting and characterizing its possible

singularities. The discrete wavelet transform (DWT) allows an orthonormal projection on a minimal number of independent modes, which might be used to compute or model the turbulent flow dynamics in a better way than with Fourier modes [11].

Despite its fundamentals and concept are dated back to Haar (1909) [17], the wavelet transform method has been accurately described and introduced by Morlet, Grossmann and Meyer only a few decades ago (1980 [35]). The scale decomposition, of an integrable function with zero mean, is obtained by the translation and dilation of only one "*mother wavelet*" function. Consequently, all analysing wavelets should therefore be mutually similar, namely scale covariant with one another, in particular they should have a constant number of oscillations. Thus, this dilation procedure allows an optimal compromise considering the uncertainty principle: the wavelet transforms can give good spatial resolution in the small scales as well as in the large scales.

In the next sections it will be shown how the wavelet approach, together with an appropriate threshold filter process, can lead to a selective separation of acoustic and hydrodynamic pressures, without any *a priori* definition of their frequency content. Since the original method formulation, improvements in efficiency and simplicity were made with the development of new algorithms for finding the appropriate threshold level, and in particular, in according to the *WT1/WT3* by Mancinelli [31] the hydrodynamic pressure is filtered out through the application of the technique proposed by Ruppert-Felsot et al. [44] for the extraction of coherent structures in a vorticity field. The application of such a procedure requires two microphones in the near field, for the WT1 procedure, and only one for a WT3 wavelet transform filtering method.

2.5.2 Method

The separation between hydrodynamic and acoustic components of the near-field pressure is based on the application of the wavelet transform to pressure signals. A detailed and complete guide for wavelet transforms, its limitations and properties is published by authors such as Farge1992 [11], Daubechies1992 [9], Meyer1993 [33], and only key aspects will be covered in this document.

The continuous wavelet transform (CWT) of a pressure time signal consists of a projection over a basis of compact support functions obtained by dilations and translations of the *mother wavelet* $\Psi(t)$, localized both in the physical and transformed spaces, the resulting wavelet coefficients result functions of the time and of the spatial scale. According to [15], the CWT of a time signal can be defined as follows:

$$w_p(s,t) = C_\Psi^{-1/2} \int_{-\infty}^{+\infty} p(\tau)\Psi^* \left(\frac{t-\tau}{s} \right) d\tau \tag{2.42}$$

with C_Ψ a coefficient that takes into account the mean value of the mother wavelet, and Ψ^* its complex conjugate scaled by s and translated by τ, while the integral represents a convolution between $p(t)$ and $\Psi^*(t)$

$$C_\Psi = (2\pi)^n \int_{\mathbf{R}^n} |\hat{\Psi}(\mathbf{k})|^2 \frac{d^n\mathbf{k}}{|\mathbf{k}|^n} < \infty \tag{2.43}$$

$$\hat{\Psi}(\mathbf{k}) = (2\pi)^{-n} \int_{\mathbf{R}^n} \Psi(\mathbf{x}) e^{-i\mathbf{k}\cdot\mathbf{x}} d^n\mathbf{x} \tag{2.44}$$

n being the number of spatial dimensions.If $\Psi(\mathbf{x})$ is integrable, this actually implies that it has zero mean

$$\int_{\mathbf{R}^n} \Psi(\mathbf{x}) d^n\mathbf{x} = 0$$

As it is computationally unfeasible to analyse a signal using all wavelet coefficients, instead of using a continuous wavelet transform (CWT), which operates on all possible scales and translations, a discrete wavelet transform (DWT), which relies on a discrete subset of values, can be performed in order to decompose the pressure signal. Arranging the scales e.g. $s_j = 2^j$ (dyadic distribution) and considering translations multiples of the scale s_j, the orthonormal basis $\psi(t)$, obtained by dilations and translations of the mother wavelet $\Psi(t)$ can be represented in the following manner

$$\psi_{[k]}^{(j)}(t) = 2^{-j/2}\Psi\left(\frac{t - 2^j k}{2^j}\right) \tag{2.45}$$

The discrete wavelet coefficients are obtained as follows:

$$w_p^{(s)}(n) = \sum_{k=-\infty}^{+\infty} \Psi^{(s)}(n - 2^s k) p(k) \tag{2.46}$$

s will represent now, the discretized scales, and $\Psi^{(s)}(n-2^s k)$ the discretized version[14] of $\Psi^{(s)}(t) = 2^{-s/2}\Psi(t/2^s)$ [4].

With the current approach, it is assumed that the hydrodynamic component of the near-field pressure, being related to coherent localized vortices, compresses well onto the wavelet basis. The component of the signal associated with the hydrodynamic pressure can be extracted by selecting the wavelet coefficients exceeding, in absolute value, a proper threshold, and the remaining part of the signal can be assumed as gaussian component, or in this case, the acoustic pressure. It appears clear that the selection of the threshold

[14] In the present approach, the wavelet transform is performed using an orthogonal wavelet basis to ensure the reversibility condition and the wavelet kernel used is the Daubechies–12 type.

represents a crucial step in the separation procedure, and its selection has to be related to physical properties, e.g. coherence and gaussianity, of the signal's components, e.g. static pressure. An initial guess for the threshold value T_0 is required, based on statistical reasoning introduced in the de-noising procedure [10]

$$T_0 = \sqrt{2\langle p'^2 \rangle \log_2 N_s} \tag{2.47}$$

with $\langle p'^2 \rangle$ indicating the variance of the pressure signal and N_s the number of samples. The threshold is discretely changed until a proper convergence criterion capturing the hydrodynamic or acoustic nature of the separated signals is satisfied.

2.5.3 *WT1* Algorithm

The following signal's components separation technique, "Wavelet Transform 1", is based on continuous comparison of the computed wavelet coefficients and iterative update of the threshold based on cross-correlation between the measured pressure in the near-field with the one delivered in the far-field. This method requires the presence of two microphone probes respectively in the near and the far fields to determine the relation of the signals. The fundamental hypothesis of this approach is that the amplitude of hydrodynamic oscillations decreases rapidly as a function of the distance from the source region, hence only the acoustic component is able to reach the far-field obtaining in this way a high cross-correlation value.

The starting point is, once selected the initial threshold value T_0, this one is iteratively adapted after an optimization method based on the gradient in order to reach the peak of the cross-correlation between the registered "noise", in the far-field, and acoustic pressure in the near field, considering everything that appears under the selected threshold value as hydrodynamic, low energy, oscillations. Once the convergence criterion is satisfied, the coherent and gaussian, e.g. acoustic and hydrodynamic pressures are considered successfully separated.

Simulation Setup and Data

3.1 Acoustic Liners: Simulation data

The main experiment, simulation of acoustic liners functioning in different regimes, is used as source data for the analyses with different methods formerly presented. The simulation is conducted in a rectangular section duct with length $L = 14400mm$, height $H = 40mm$ and width $W = 12mm$. The array of acoustic liners is composed of 11 square section cavities of width $w = 10mm$ and height $h = 38.61mm$, communicating with the duct through 8 orifices of diameter $d = 1.3mm$. The array is positioned, by considering the left border of the first (in order from left to right) liner as the center of the local reference coordinate system $\mathbf{X}(X,Y,Z)$, at $x = 7125mm \equiv \mathbf{X} = (0,0,0)$.

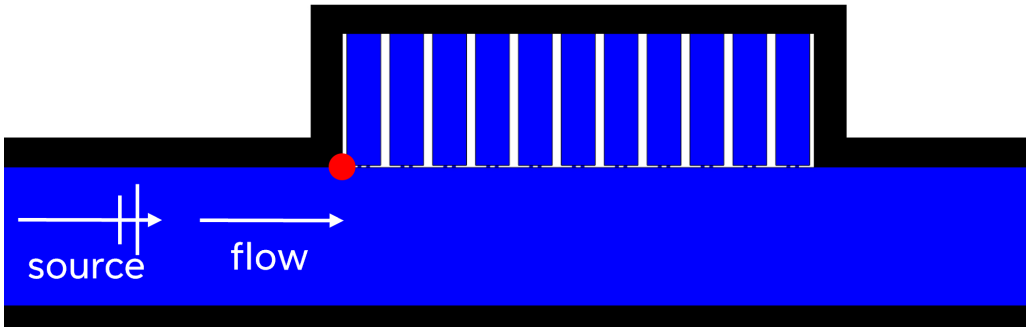

Fig. 3.10 Z-Plane section of the liners computational domain view. Also are indicated the direction of the flow (*flow*), acoustic waves (*source*) and the red point to indicate the origin of the coordinate system $\mathbf{X}$.

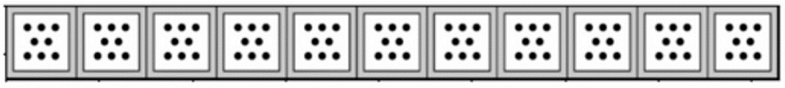

Fig. 3.11 Representation of orifices of each cavity disposition on the faceplate.

The main experiment is conducted for different conditions of flow and acoustical sources power and frequency to adequately simulate different behaviors of the liners' damping, e.g. linear and non-linear, as well as frequency dependency regimes. The initial intentions were to analyze all the flow solutions in different conditions, but several major limitations were faced:

- SPOD and Wavelet analyses require, in first place, an enormous amount of operative memory, processing units and relative storage to process data (this issue was partially solved by relying on the computational power provided by HPC [42]), and secondly, even possessing the necessary computational power, the analyses time and successful result remains an open question.
- in order to obtain good results, the solutions data required a significant amount of storage and time to process because of the intrinsic difficulty of the adopted method, lattice Boltzmann methods (LBM), and different stages of grid refinement submitted.

Hence, available data for the analyses sees the simulation of the duct with liners at the resonance frequency $f = 1400Hz$ and with high amplitude source waves $SPL = 145dB$, in flow and no-flow conditions, by denoting the no-flow condition as zero-valued Mach number, $M = 0$, and as $M = 0.3$ a turbulent flow situation, it is schematically reported in the following Table 3.1. It is worth mentioning that two different solutions were available, but their conditions can hardly relate to each other and to the examined ones to obtain significant and unequivocal comparisons and considerations.

flow Mach	SPL	source frequency	number of snapshots	sampling frequency
$M = 0$	$145dB$	$f = 1400Hz$	$N_T = 6321$	$f_s = 421.86kHz$
$M = 0.3$	$145dB$	$f = 1400Hz$	$N_T = 4741$	$f_s = 421.86kHz$

Table 3.1 Analyzed simulations main parameters.

We can observe from the “snapshots”, instantaneous flow fields, the Figure 3.12 refers to a generic instantaneous flow field generated in the duct without the mean “grazing” flow. Event thou, the high amplitude waves ($SPL = 145$) let the liners work in non-linear regime, its functioning is clearly observable from the strong attenuation after the liners array containing section (“main” region of interest). In the case of a $M = 0.3$ mean turbulent flow, Figure 3.13, definitely the attenuation occurs but weaker, and it is difficult to assign the exact function to every point, also more dynamics are observable near the proximity of orifices region.

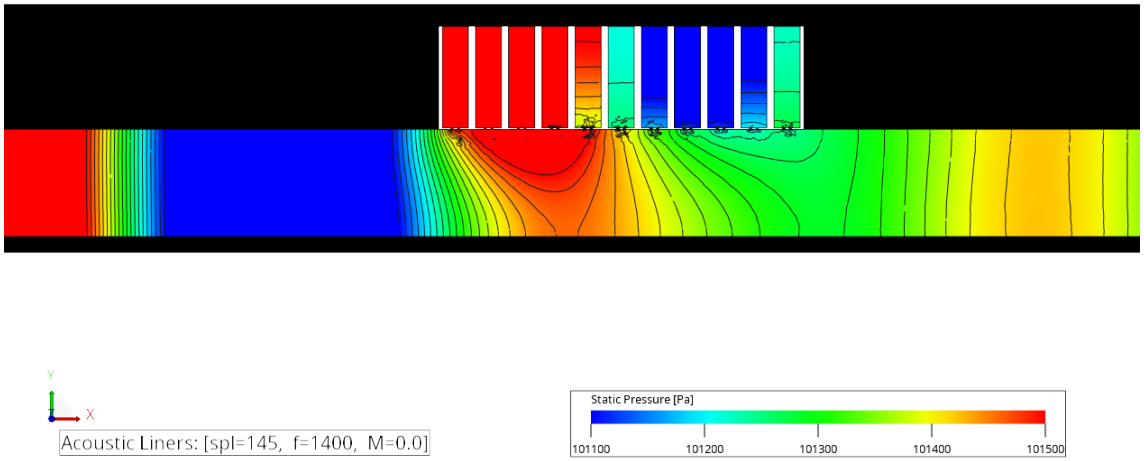

Fig. 3.12 Z-Plane section, $M = 0$: generic instantaneous static pressure field of the liners computational domain view.

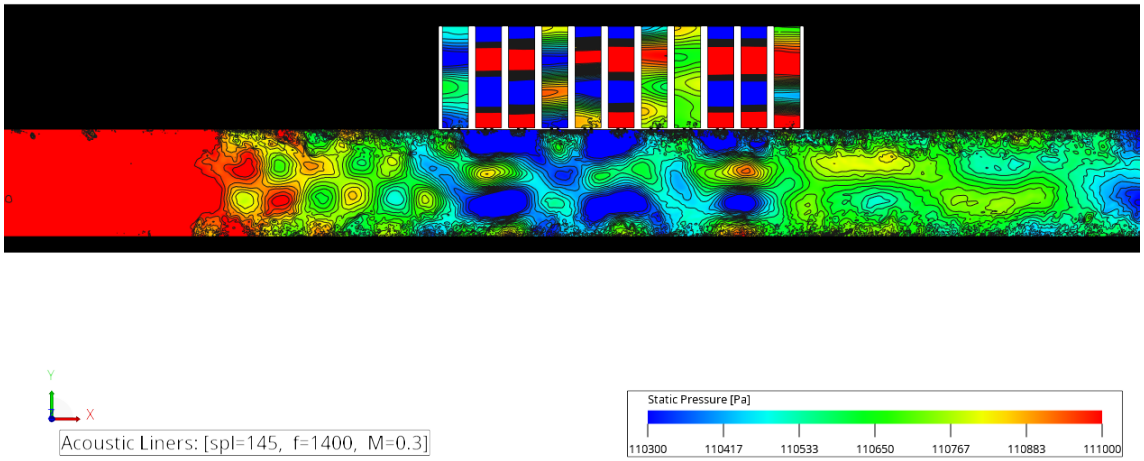

Fig. 3.13 Z-Plane section, $M = 0.3$: generic instantaneous static pressure field of the liners computational domain view.

3.2 Spectral analysis

The first step, before executing a Spectral POD analysis, is to preview what useful information is obtainable with traditional "classic" analysis methods, e.g. the pressure signal analysis, SPL calculation and power spectral analysis.

Static pressure signal was sampled for the whole solution duration in discrete points along the X axis of the duct (Figure 3.14): 643 points in $X = (-0.5, 0.5)m$ and in three sections before, in occurrence of and after the liners section (Figure 3.15):3 sections located at $X = [-0.05, 0.068, 0.186]m$ and in 7 points $Y = [-0.005, -0.010, -0.015, -0.020, -0.025, -0.030, -0.035$

The first information acquired is that the pressure field (and the whole flow field variables), present a transitory effect before the source's waves arrive in the liners region

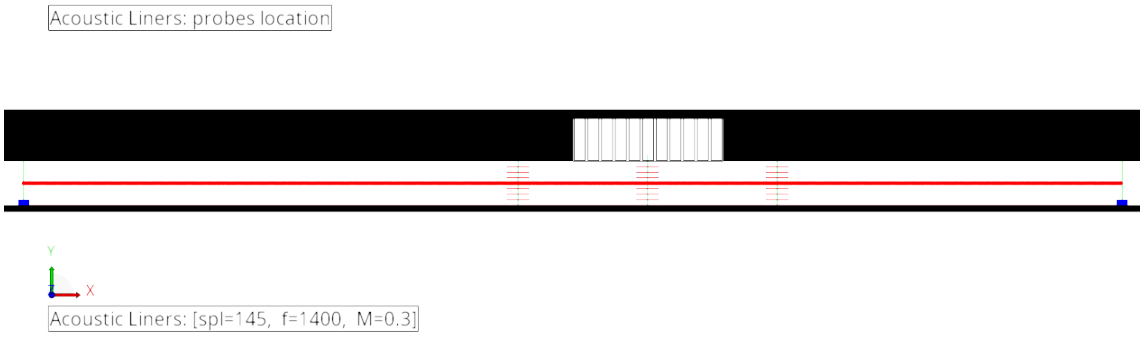

Fig. 3.14 Surface plane (probe plane), used for measurement of pressure along the duct axis.

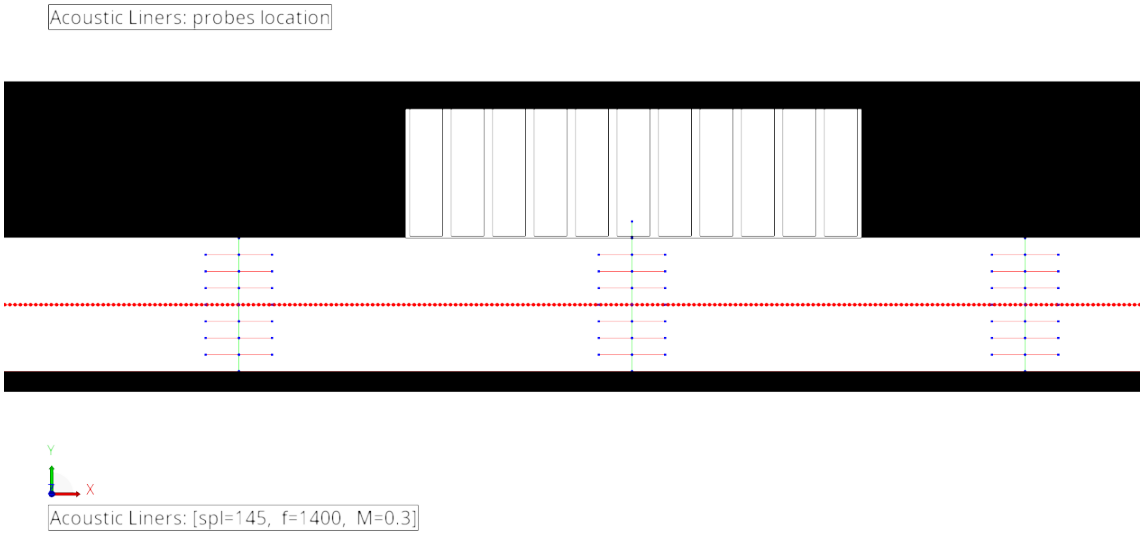

Fig. 3.15 Section probes used for measurement of pressure in the duct's reference sections (inlet, main, outlet).

and after the last traveling wave passes the *main* section. Hence, a trimming operation was executed for the pressure signals and the new beginning and ending frames for the next analysis were set. After this preliminary trim operation (and also before trimming), the two solution data available from the main experiment simulations, $M = 0$ and $M = 0.3$ with $SPL = 145dB$ and forcing frequency $f = 1400Hz$, had a slightly different snapshot amount (duration), to compensate this difference and work on data in "same conditions", a second trim operation was executed to equalize the content to analyze. Final length is of $N_T = 4000$ frames per both the flow field solutions. In Figure 3.16 (and in every other successive graphs in this document) the set color scheme refers with "blue" color to the $M = 0$ condition and the "red" to the $M = 0.3$ condition.

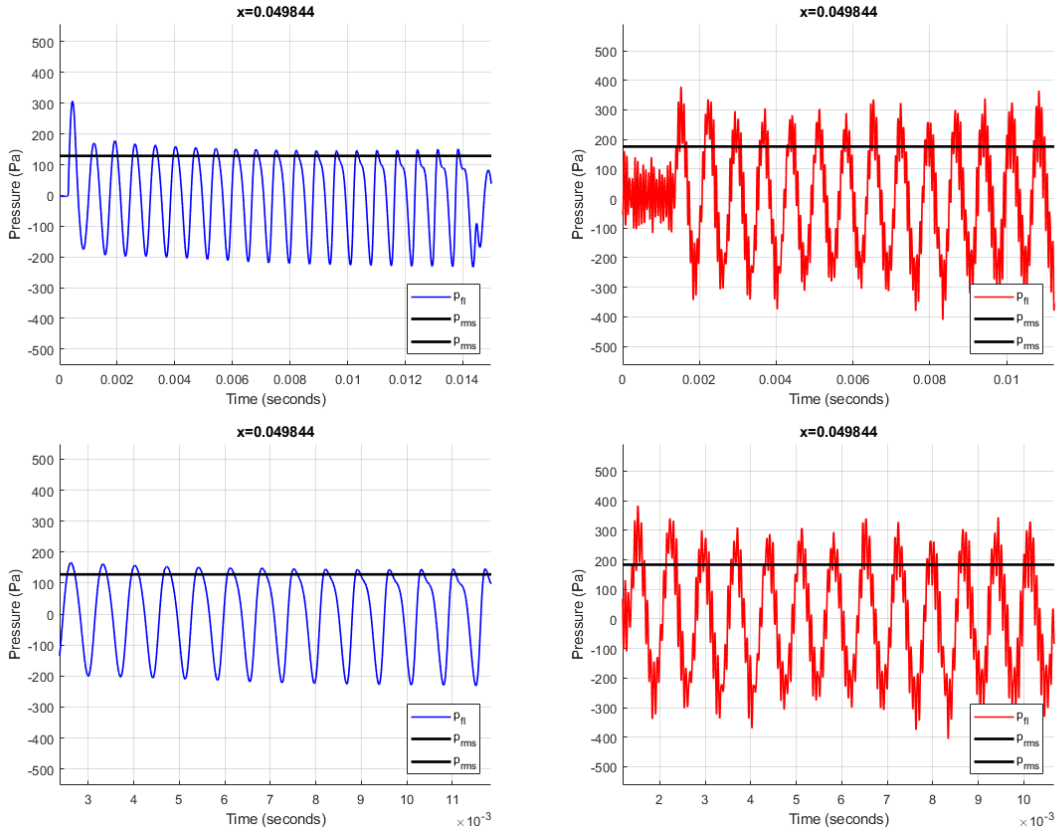

Fig. 3.16 Pressure data, before and after trim operation. It can be observed that before the trim operation both the signals, the blue and the red one (referring to the "no-flow" and "flow" conditions respectively), present a transitory period, the same phenomenon is present in the ending (*outlet*) sections, determining the time when the wave's train ends.

3.3 SPOD: analysis parameters

The SPOD reveals itself very computational- (and even more memory-) power demanding operation, for this purpose, the resources of the HPCPolito [42] were successfully borrowed and used. Apart from the necessary "power" to execute the spectral POD, a high sensitivity on input parameters was registered and accounted for, in the operation submission phase. The input is divided into three sections:

- The power request section, managed by SLURM ("Job Scheduler" of HPCPolito).
- The spectral analysis input section, with parameters influencing the spectral analysis such as bandwidth, minimum and maximum frequency and frames used for the analysis, and overlap factor for Welch average method.
- The SPOD section, referring to the requested number of modes extracted, the Cartesian extraction blocks determination and the mesh size.

3.3.1 Regions of interest determination

Since the first attempts to execute the SPOD it appeared necessary to divide the whole analysis into several *regions of interest* (ROI), the issue is that the SPOD of the whole domain necessitates enormous amount of operating memory allocation[15], and moreover the scales and dynamics involved in such a big area are either lost (or integrated) or covered by the greater (more energetic) scales dynamics. Even by increasing the memory allocation, calculation time and requesting the very fine mesh of analysis, the final result is still relying on the input file timeframe, which is not sufficient for a high-resolution, in frequency and in space, analysis.

To overcome this issue, a very reasonable solution was to divide the whole flow field domain into sub areas (this denomination, will be kept in the next chapters referring to SPOD analysis):

- *full*: the first SPOD ROI, analyzing the whole flow field domain with "great" resources demanding workload.
- *inlet*: duct section before the liners array area.
- *main*: duct section "under" the liners array.
- *outlet*: duct section after the liners array region.
- *liners*: liners cavities area.
- *orifices*: 11 square areas comprehending only the orifices of each liner.

ROI	**width *[m]***	**height *[m]***	***X*-center *[m]***	***Y*-center *[m]***	**mesh *[m]***
full	0.300	0.08	0.050	0.00	0.0010
inlet	0.100	0.04	-0.050	-0.02	0.0003
main	0.136	0.04	0.068	-0.02	0.0003
outlet	0.064	0.04	0.168	-0.02	0.0003
liners	0.136	0.04	0.168	0.02	0.0003
orifices	0.010	0.01	**liners**	0.00	0.0001

Table 3.2 SPOD: ROI determination and geometrical parameters used for analysis. For orifices X center, as the whole *orifices* ROI is composed of 11 square blocks, the location of liners reference X position was used for their center determination.

[15] During the "full" (coarse) domain analysis, the requested power was of 32 CPUs with 64 GB of RAM each

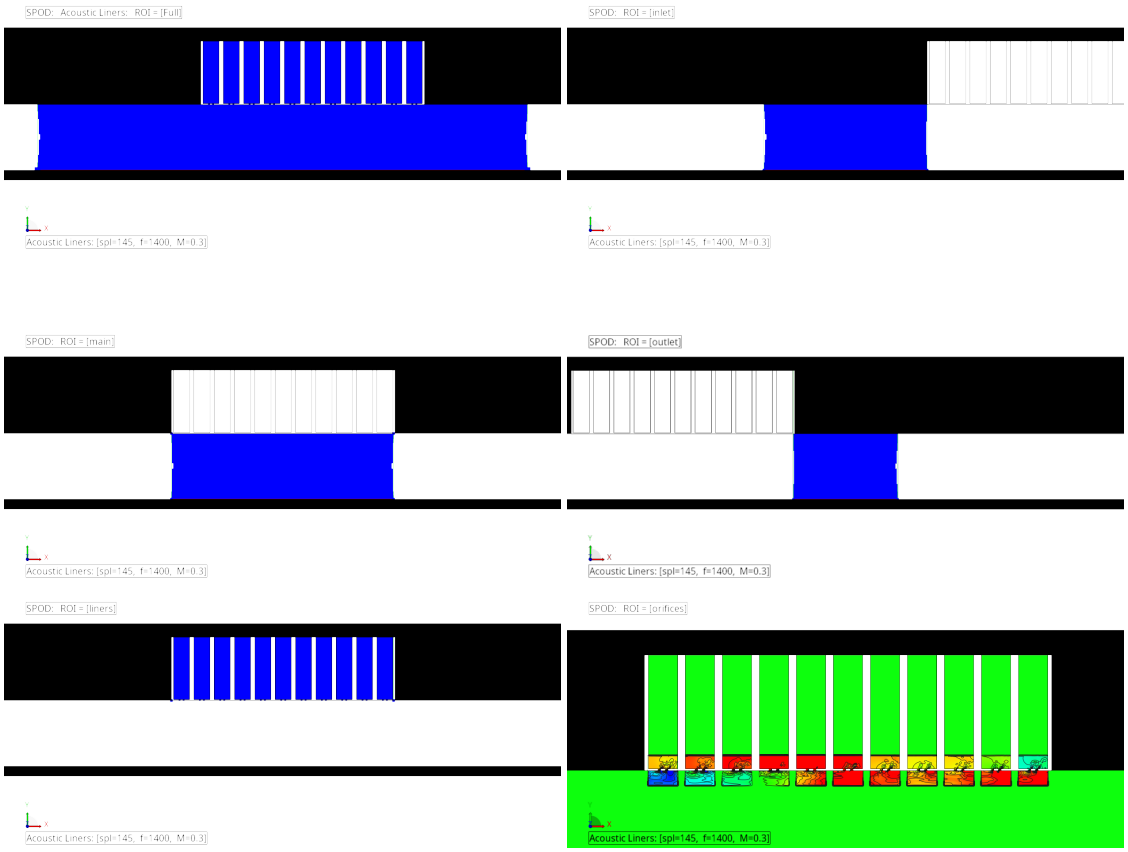

Fig. 3.17 SPOD Analysis, regions of interest (ROI) definition.

3.3.2 Input Parameters

The key parameters to influence the successful termination of the SPOD analysis are those used to define the spectral analysis, as they directly influence the cross-spectral density matrix definition and amount of "blocks" used during the Welch's spectral analysis method Parameters and reasons for using them during the SPOD analysis, as well as region of interest subdivision and purpose.

Accordingly to the Equation 2.26, once the available N_T snapshots are determined and the N_{ov} of overlapping frames is set (optimal value is overlap factor of $N_{ov}/N_f = 0.5$, but this can slightly change in order to make use all of the available frames), the only "free" parameters are the number of blocks N_b and the number of frames per each block N_f.

The necessary N_f is determined, according to Equation 2.41, by the sampling frequency f_s and the desired frequency resolution (bin size). Our intent is to have the maximum possible frequency resolution, corresponding to the minimum bin size (Δf), to have the most detailed spectral information (by sacrificing in this way the block average operation). Hence, having the limiting available number of frames (also trimmed to cut off the transitory effects and equalized in duration), the minimum allowable $\Delta f = 200Hz$.

3.4 Wavelet: analysis parameters

As well as for the SPOD, the Wavelet analysis relies on a very high power and memory demanding operations, firstly because the solution data is large due to the solving method used for the near-microfluid dynamic scale (in proximity of the orifices, also considering the non-linear regimes), also the "Opty-dB's" analysis algorithm executes the `hydrofilter` (the operation denominated and designated for the wavelet transform analysis and decomposition) on the whole domain without consenting the choice of *regions of interest*, as in the SPOD's case. Alternatively, it was possible to divide the complete solution file into several spatially cropped sub-data, but this kind of operation seemed to be more appropriate for an intensive (spatially localized) analysis with different techniques set-up *ad hoc* for the purpose and not an investigation on different methods like this one.

The number of the wavelet coefficients, commonly named the *wavelet mother function* type, is set to 12 [31], and the factor of the threshold coefficient (necessary during the use of the iterative algorithm) to unitary, by setting this value higher or lower would imply transferring some wavelet series terms, and in consequence assigning more or less energy content, to the Coherent or to the Gaussian contributions.

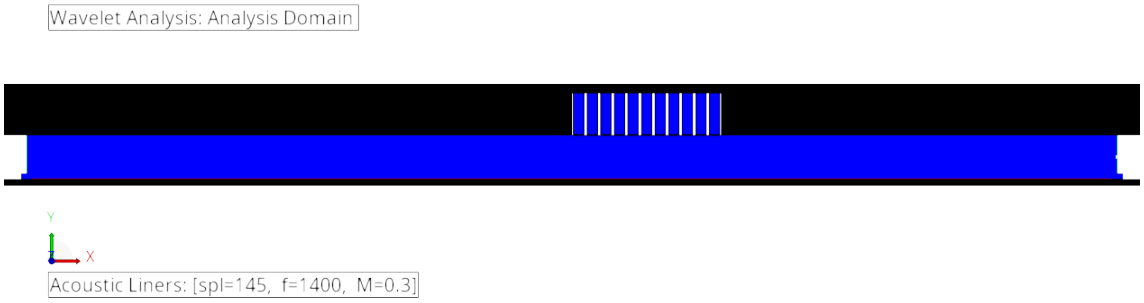

Fig. 3.18 Wavelet analysis, region of solution domain used for wavelet transform analysis.

The first attempts to execute the wavelet transform and decomposition were conducted by using the same spectral parameters as in the case of the SPOD (in the first place to make some considerations on data analyzed in the "same conditions"), but unfortunately the highest obtainable frequency resolution was with bands of $\Delta f = 300Hz$ (a slightly broader spectral content is to expect).

The wavelet transform "WT1" technique [31], necessitates of a microphone probe positioned in a way to capture the acoustic signal in order to correlate it to the pressure fluctuations recorded in the fluid domain. The most suitable location was considered to be in the *outlet* region (in the area after the waves pass the liners array), exactly located at $X = 186mm$ and on the axis of the duct $Y = -0.02$ (center of the *outlet* ROI), Figure 3.19.

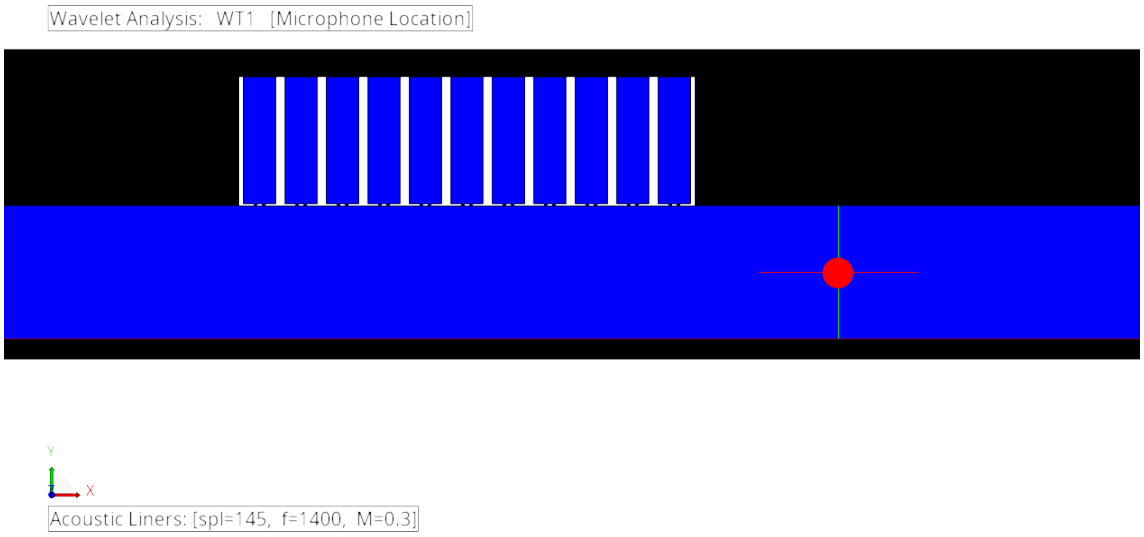

Fig. 3.19 Wavelet analysis, microphone probe location used for WT1 method.

Results analysis

4.1 Spectral analysis

4.1.1 Data overview

The first results to be observed, are the 3D representations of the pressure fluctuations along the axis of the duct, Figures 4.20 reporting the “no-flow” (only acoustics) condition, and 4.21 for the turbulent flow $M = 0.3$ condition. The “smoothness” of the pressure time history without the presence of the grazing flow, indicates the absence of turbulent pressure fluctuations due to the stationarity of the flow field. Also, it is very clear the amount of damping in the post-liners area and the regularity of the oscillations, unlike the case of the “flow” condition (Figure 4.21) where the spikes indicate the random nature of turbulent flow. Also, in the case of grazing flow, even at preliminary point, is observable that the attenuation deriving from the liners presence, is present but much lower in comparison to the only-acoustics.

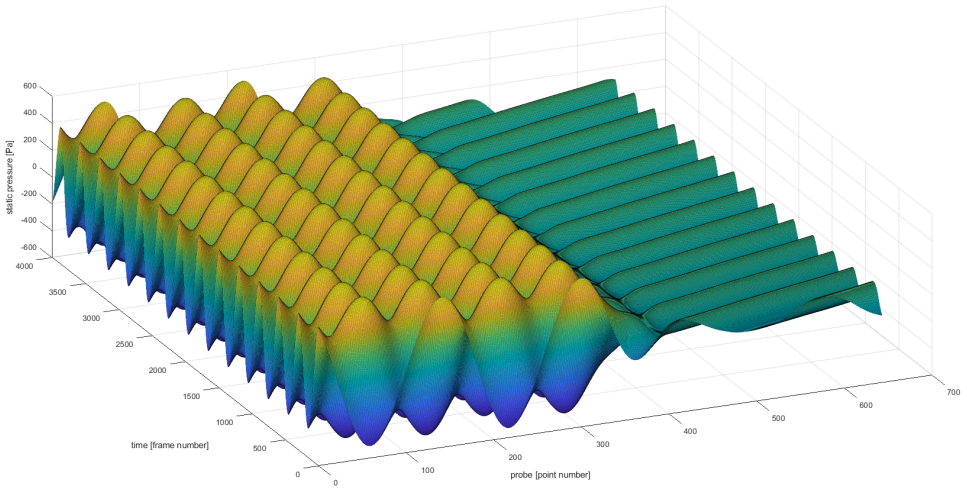

Fig. 4.20 $M = 0$: Acquired pressure 3D visualization.

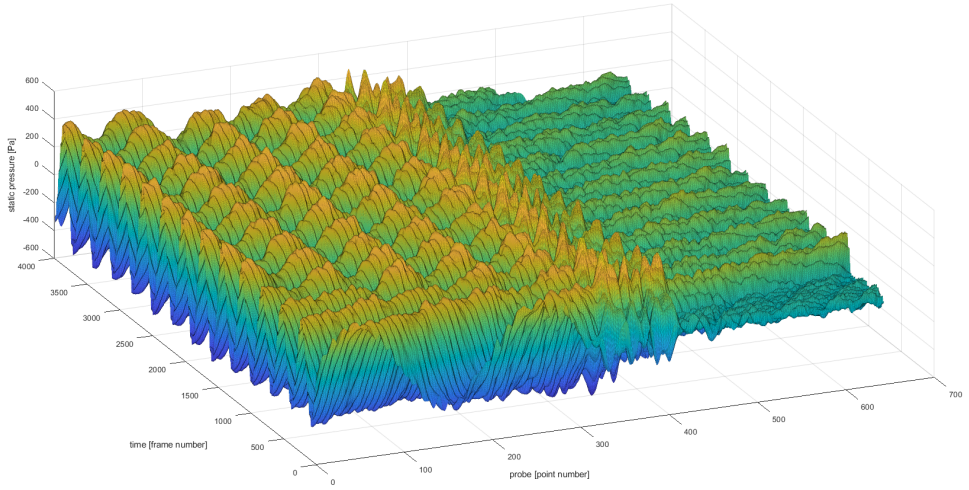

Fig. 4.21 $M = 0.3$: Acquired pressure 3D visualization.

4.1.2 Pressure signal

The pressure signal acquired from the probe surfaces, is here reported only for 6 points corresponding to key locations: $X \approx -0.05m$, $X = 0m$, $X \approx 0.05m$, $X \approx 0.10m$, $X \approx 0.137$ and $X \approx 0.185$. Each of these points represents dynamically significant locations: the center of the *inlet*, the edge of the liners' *main* area, two of its internal points, and its terminal point, and the center of the *outlet*.

The first thing to observe, is that, as expected, the pressure in case of the absence of flow, Figure 4.22 is smooth and only perturbed by the passage of the forcing wave. It presents higher *rms* value and higher peaks in the *inlet* region, after the middle of the liners area, most of the acoustical energy seems depleted and remains constant until the exit. An additional and not completely described effect is visible from the liners area and advancing, the liners' presence induces a second wave (probably after that a "double reflected" wave is transmitted) that appears to have the same frequency but an offset phase to the main forcing waves train, also interesting to observe that the second wave seems to increase in time (as to indicate the cumulative residual energy).

For the flow ("red") condition (Figure 4.23), two main behaviors are observed: the spikes observed in the Figure 4.21, appear to have a specific high-frequency content along the whole duct extension (at certain locations these seem to increase in amplitude e.g. at $X \approx 0.01m$); secondly, unlike for the case of the "no-flow" condition, the *rms* value (and consequently the amplitude of the waves) doesn't seem to decrease monotonically through the duct.

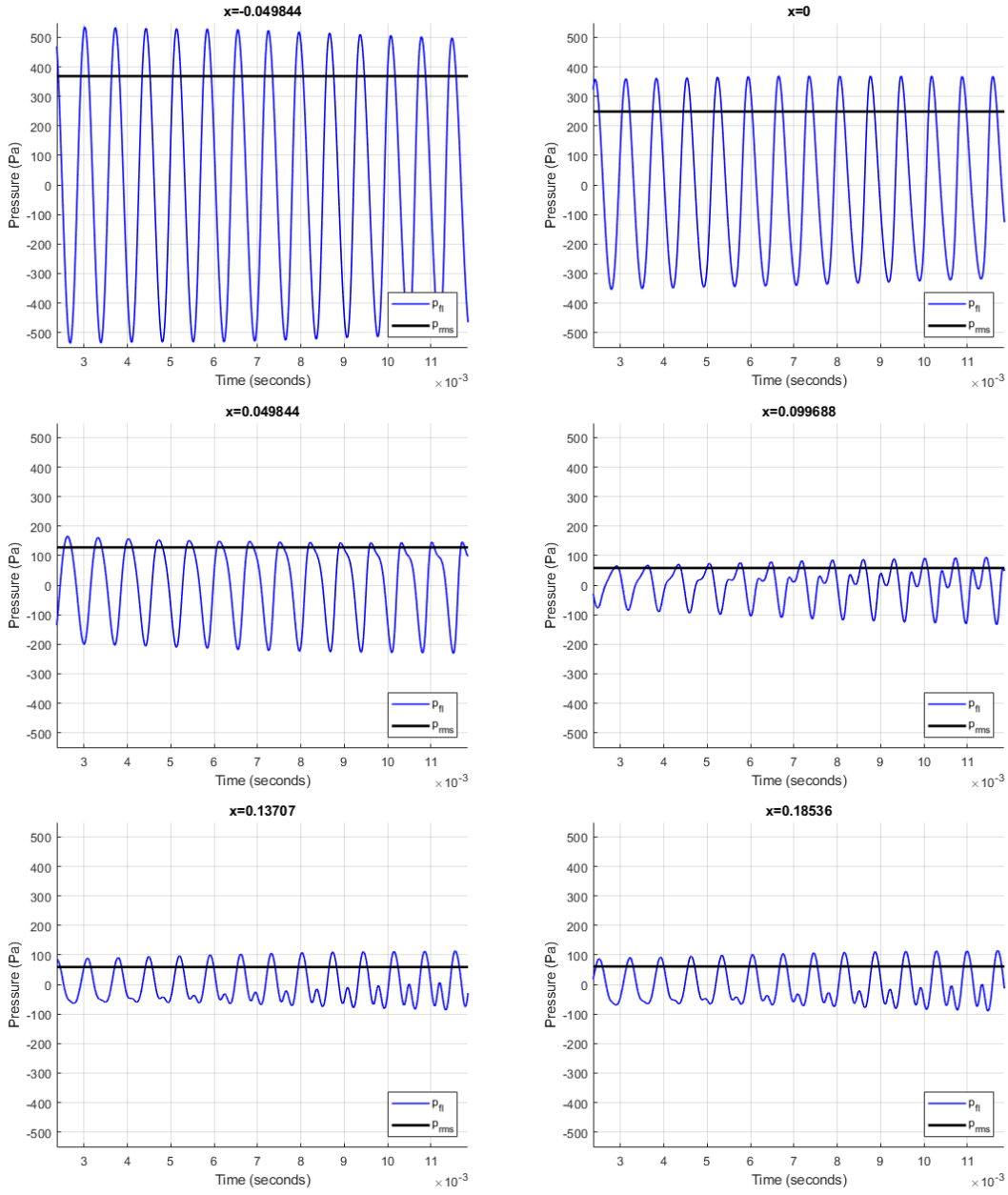

Fig. 4.22 $M = 0$: Pressure signal data acquired in key locations(after trim operation).

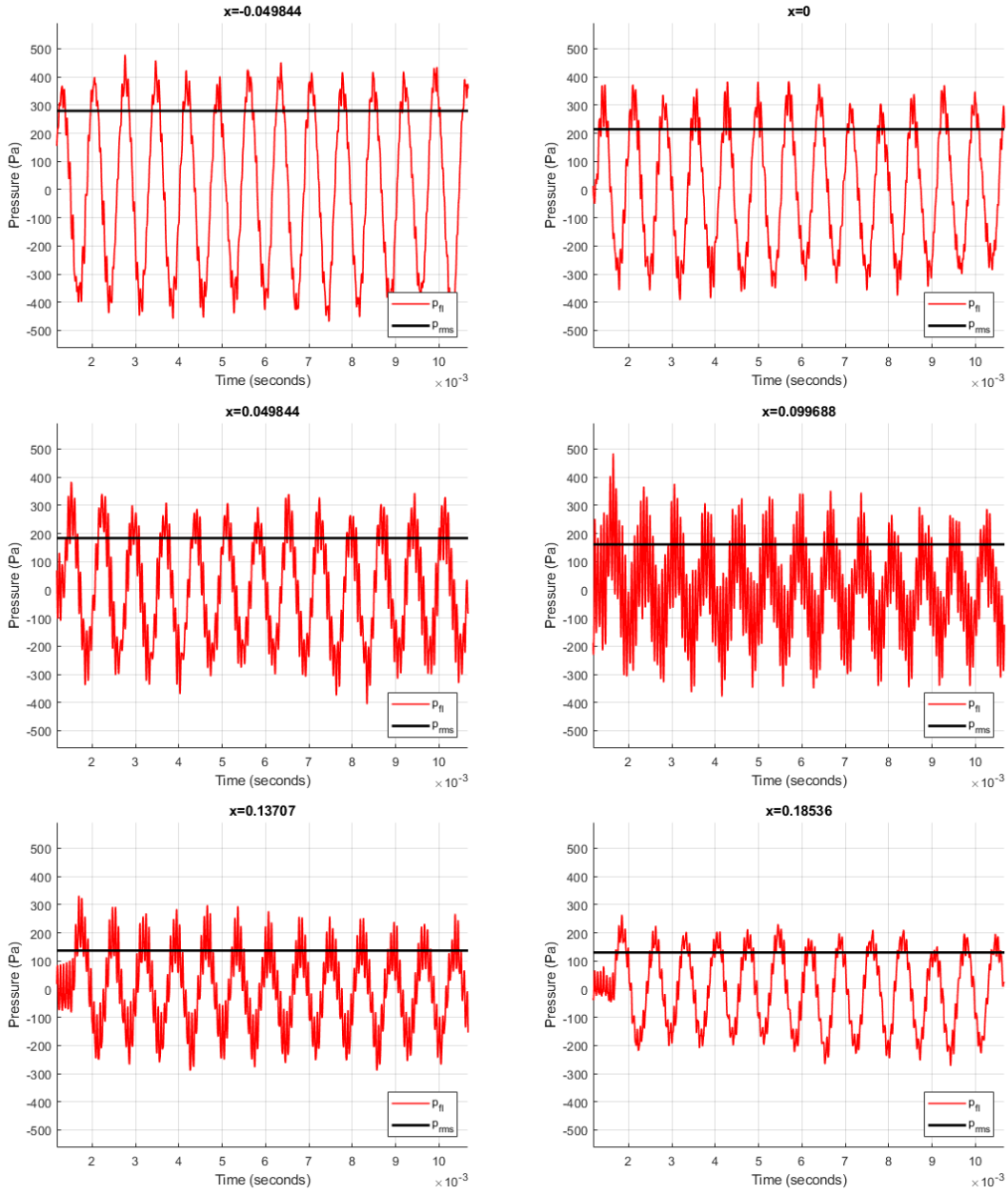

Fig. 4.23 $M = 0.3$: Pressure signal data acquired in key locations (after trim operation).

4.1.3 Sound Pressure Level: SPL

For the SPL formulation (Equation 2.10), and its successive behavior through the duct, the "standard" reference pressure was used $p_{ref} = 20\mu Pa$ of human threshold of audibility. The first thing to observe is that the SPL does not have the constant value before the liners array region, meaning that all the incoming waves have their maxima in definite locations, defined by a spatial period which appears to be shorter for the flow condition, which is an unexpected behavior considering that the two experiments conducted in the same conditions (apart from the flow presence).

The boundary conditions include that both the experiments must have the same power forcing wave, $SPL = 145dB$ and at the same frequency $f = 1400Hz$, but what is evident is that for the case of the grazing flow condition, before reaching the liners area, the maximum registered SPL is few dB lower than the expected and respected by the blue condition, and the average (spatial) $SPL_{av,flow} \approx 141.3dB$.

The central part of the chart, Figure 4.24, reports the black markers to indicate the positions of the single probes reported in Figures 4.22 and 4.23 for the respective conditions (the background aids to locate relative to the duct locations). While both the experiments present a decrease in SPL due to the presence of the liners, the presence of flow does not allow the monotone local damping of the pressure e.g., there appear zones where are present local maxima, unlike for the only-acoustic condition where the decrease appears to be constant till the end of the liners' array.

The *outlet* is not supposed to alter the pressure behavior after the damping (lower for the "flow" condition) in the *main* ROI was registered. Small amplitude spatial oscillations are still visible for the "red" flow with remaining $SPL > 135dB$ while the "blue" seems to remain steady under $130dB$.

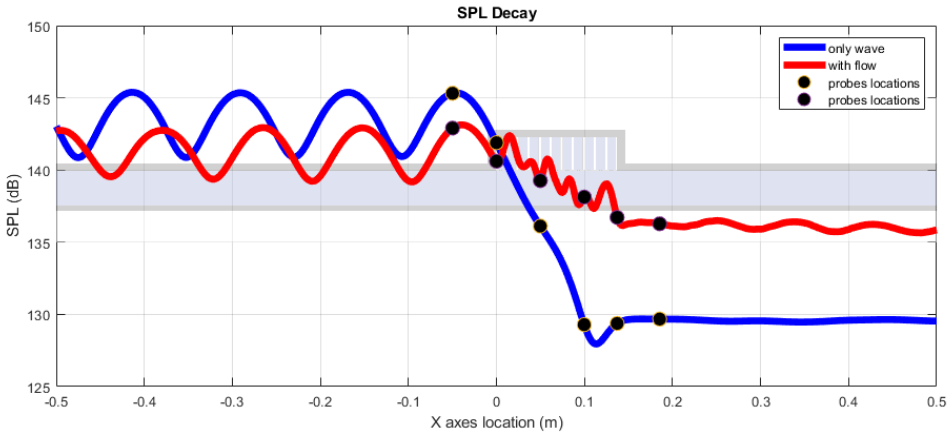

Fig. 4.24 SPL-Decay(X), full view along the duct and black markers to indicate locations of the probes used to sample pressure of Figure 4.22, 4.23.

Additional SPL measurements were conducted in the sections defined by the probes positioned as described in the previous chapter, Figure 3.15. This allowed the measurement of the cross-sectional SPL, showing a certain degree of asymmetry due to the presence of liners in the relative section, and a Y-axes variability for the flow condition.

4.1.4 Spectra

In order to extract the spectra of the simulations, several actions were taken, the first of which was dividing all the points into three groups in agreement with the precedently

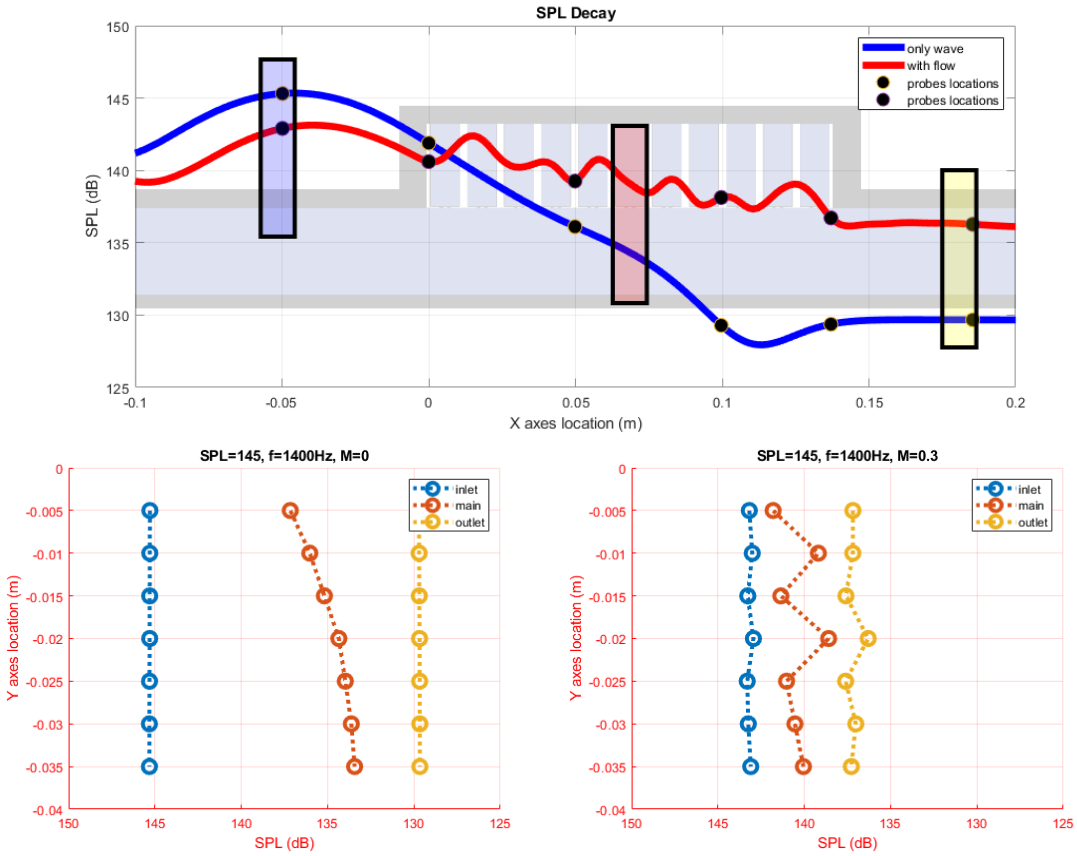

Fig. 4.25 SPL decay chart, cross-sectional measurement, in inlet, main and outlet reference sections.

explained criteria and in accordingly to the used scheme: inlet, main and outlet. Afterward, the whole the pressure signal (vector of the respective probes) was averaged with the Welch method (MATLAB function, `pwelch`).

As for the no-flow condition, there is a clean behavior due to the only acoustic phenomenons. The Spectra magnitude presents several peaks at the frequencies corresponding to the main signal and its next three harmonics. The magnitude referred to the main and outlet sections is a few orders of magnitude lower than the inlet one, Figure 4.26.

The flow condition presents the peaks corresponding to the main frequency and its next one harmonic, Figure 4.27, but are as well evident peaks at high frequency $f_t \approx 14.2kHz$ which are present in the inlet and the outlet of the duct, corresponding to the high-frequency oscillations registered in the pressure signals, due to the turbulence. These high-frequency oscillations do not appear to resent in substantial way of the liners' presence, while a small damping is present, it remains orders of magnitude higher than the second harmonic. By setting the chart range on a larger scale, it is possible to observe the typical turbulent spectra.

The spectra comparisons, Figure 4.28, highlights the power content of the two experiments before and after the liners' region. In input, both the spectra appear to have

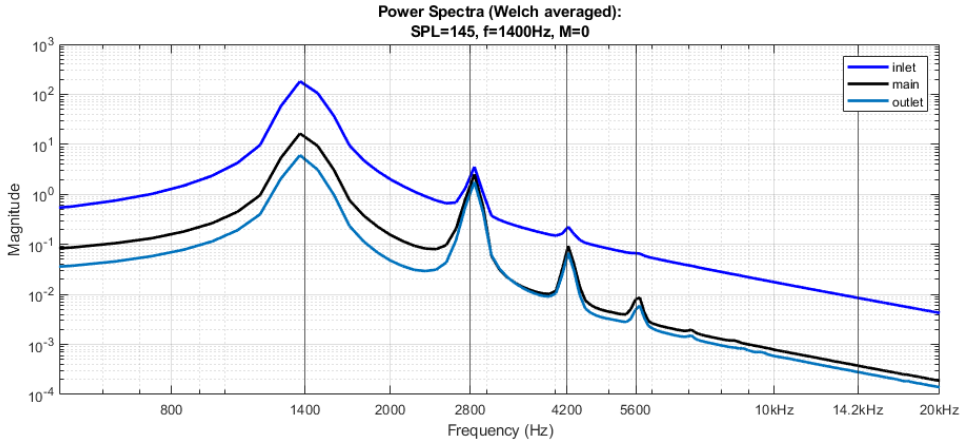

Fig. 4.26 Pressure spectra, the color scheme identifies the region in which the pressure signal was sampled and averaged.

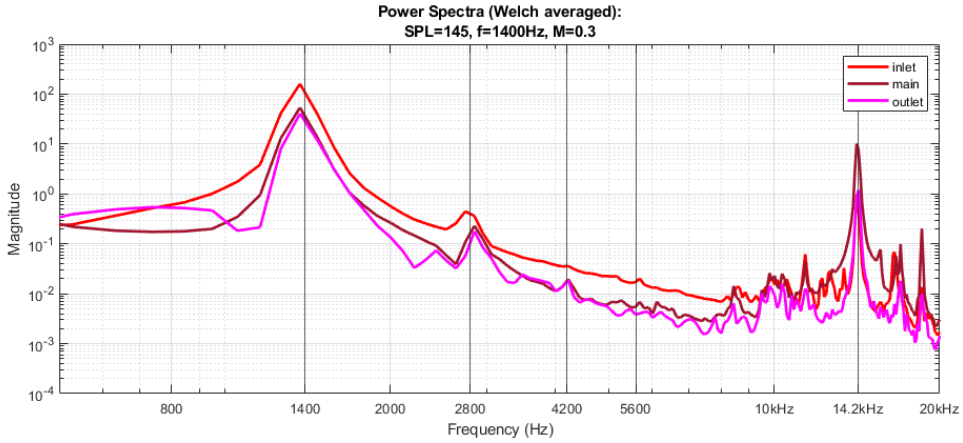

Fig. 4.27 Pressure spectra, the color scheme, identifies the region in which the pressure signal was sampled and averaged.

similar power while differently distributed due to the reasons already cited. In output, the inversion occurs, the no-flow condition presents lower power in relation to a better liners functioning.

4.2 SPOD analysis

4.2.1 Output Data

The main outputs produced by the SPOD procedure software (`Opty-dB`) consist of four sets of files:

- files containing the real part of every Fourier component of the SPOD mode of order n for the imported pressure variable. These files can be visualized via the dedicated software “PowerVIZ”, and contain the spectral content of the respective mode, e.g.

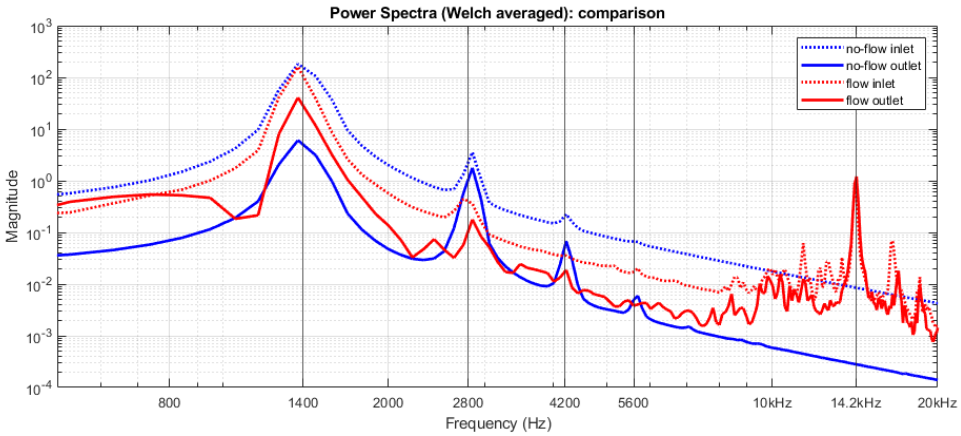

Fig. 4.28 Pressure spectra comparison, the color scheme identifies the flow condition while the line style identifies the region in which the pressure signal was sampled and averaged.

every mode visualized in the domain for the available discrete frequencies resulting from the input parameters.

- files containing the reconstructed transient solution for each extracted SPOD mode. After the extraction process completes, each mode is used for its time transient flow field.
- the matrix of containing the complex expansion coefficients $\hat{a}_j(f)$ (Equation 2.22) as well as the complex eigenvalues $\tilde{\Psi}_{f_k}$ (Equation 2.37) [45].

4.2.2 Average pressure field

Additionally, during the PCA and other decomposition techniques, the first step is to subtract the average from the flow fields (or in general matrices), so is done here, and additionally this average flow field is exported. Furthermore, the average flow field can be summed up together with the other extracted modes in order to reconstruct the initial fluid solution [53]. In the following extracted average pressure flow fields contours, it is possible to observe a minimal relative pressure changes in comparison to the standard $p_{std} = 101325Pa$ for the case of only-acoustics, and slightly greater differences smoothed by the grazing flow for the flow conditions as well as increased in the center contours for the presence of the boundary layer.

4.2.3 Modal Spectra

The extracted eigenvalues (to the eigenmodes), as expected from the SPOD spectral analysis input parameters, a maximum of 4 to 5 modes were successfully extracted, this is due to the fact that, as stated in the Chapter 2 (SPOD algorithm), the solution is obtained

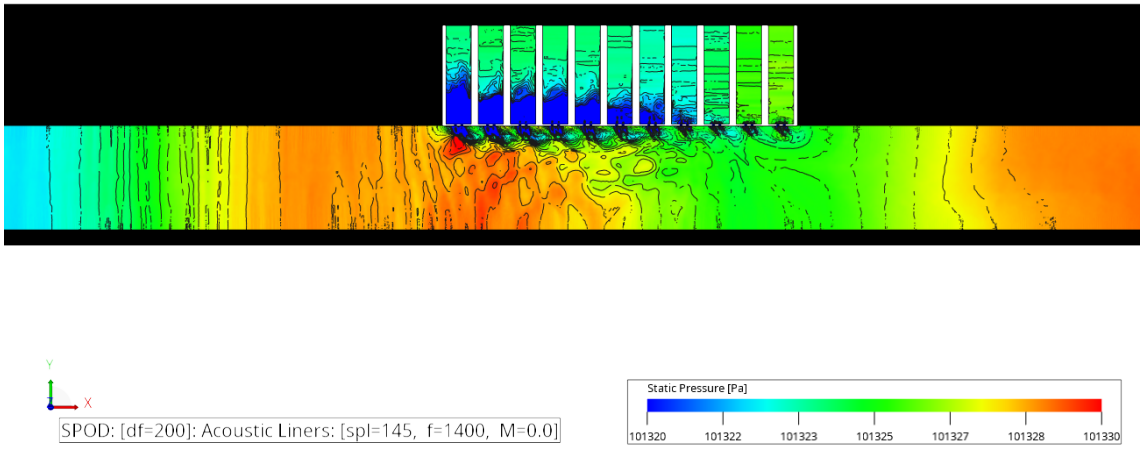

Fig. 4.29 $M = 0$: Average pressure field contour extracted.

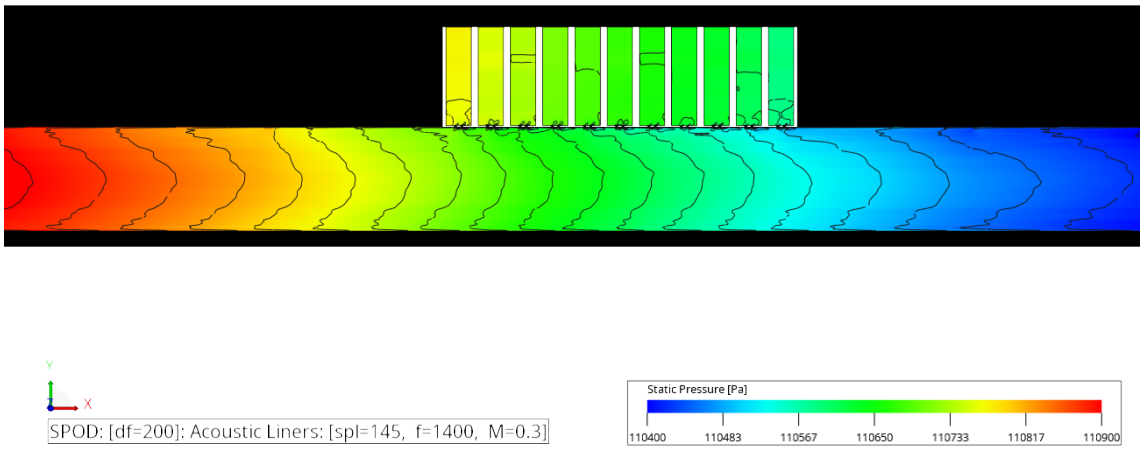

Fig. 4.30 $M = 0.3$: Average pressure field contour extracted.

by reduced extracted matrices via the “snapshot” method; hence, a maximum number of obtainable modes, and relative eigenvalues, is equal to the number of analyzed blocks, and lower scales energy content (usually supposed as noise) results integrated in the most energetically dominant modes.

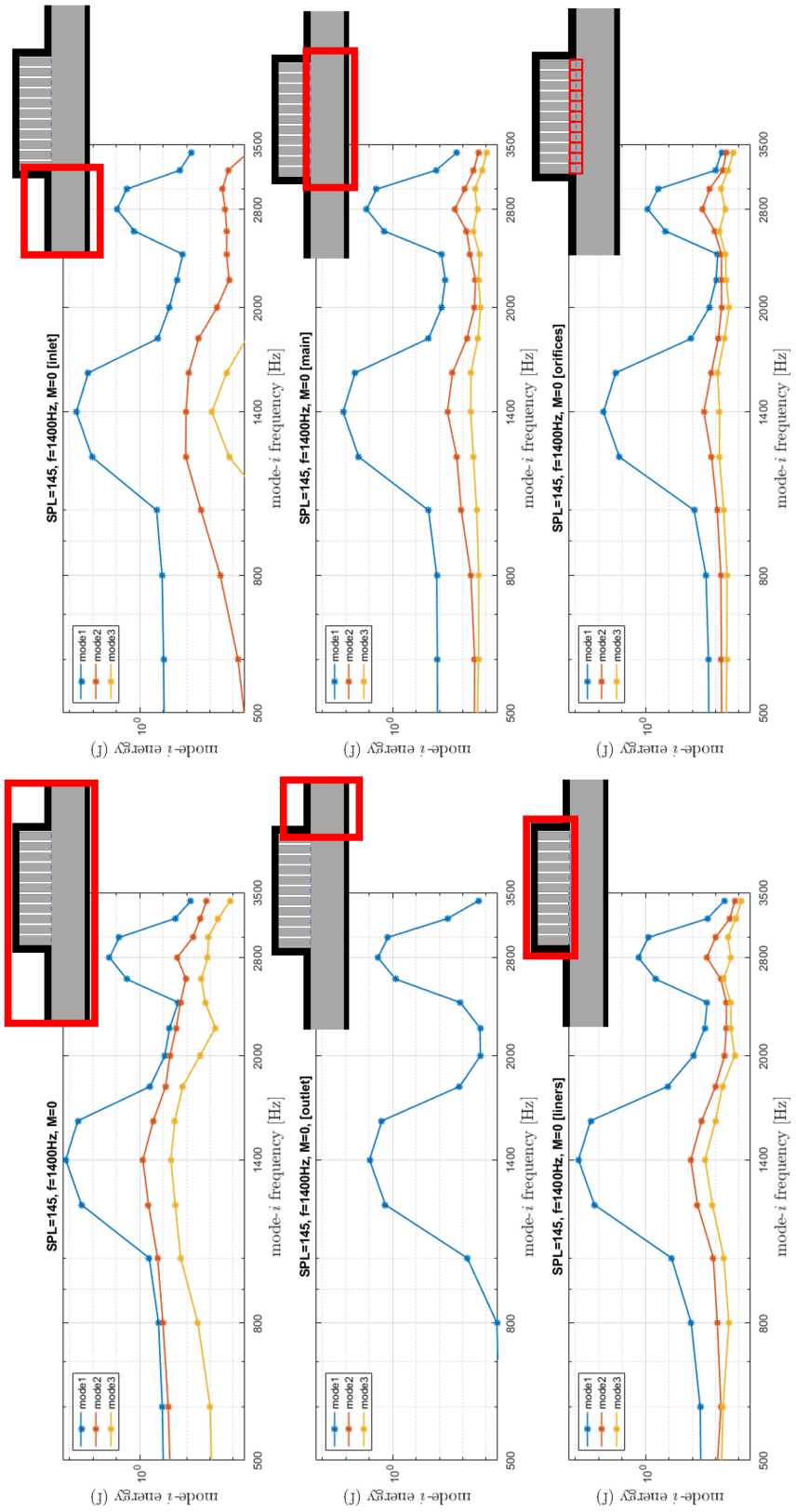

Fig. 4.31 $M = 0$: modal spectra. Only the first 3 modes are reported per each ROI (the higher order modes lay on several orders of magnitude lower scales). Only the 1^{st} mode (the most dominant) presents energy content at frequencies corresponding to the forcing wave and its harmonic. Moreover, this evidence is maintained in the whole domain and all the ROIs. After the attenuation occurs, keeping the same magnitude scales in the plot, only the first mode is observable in *outlet*.

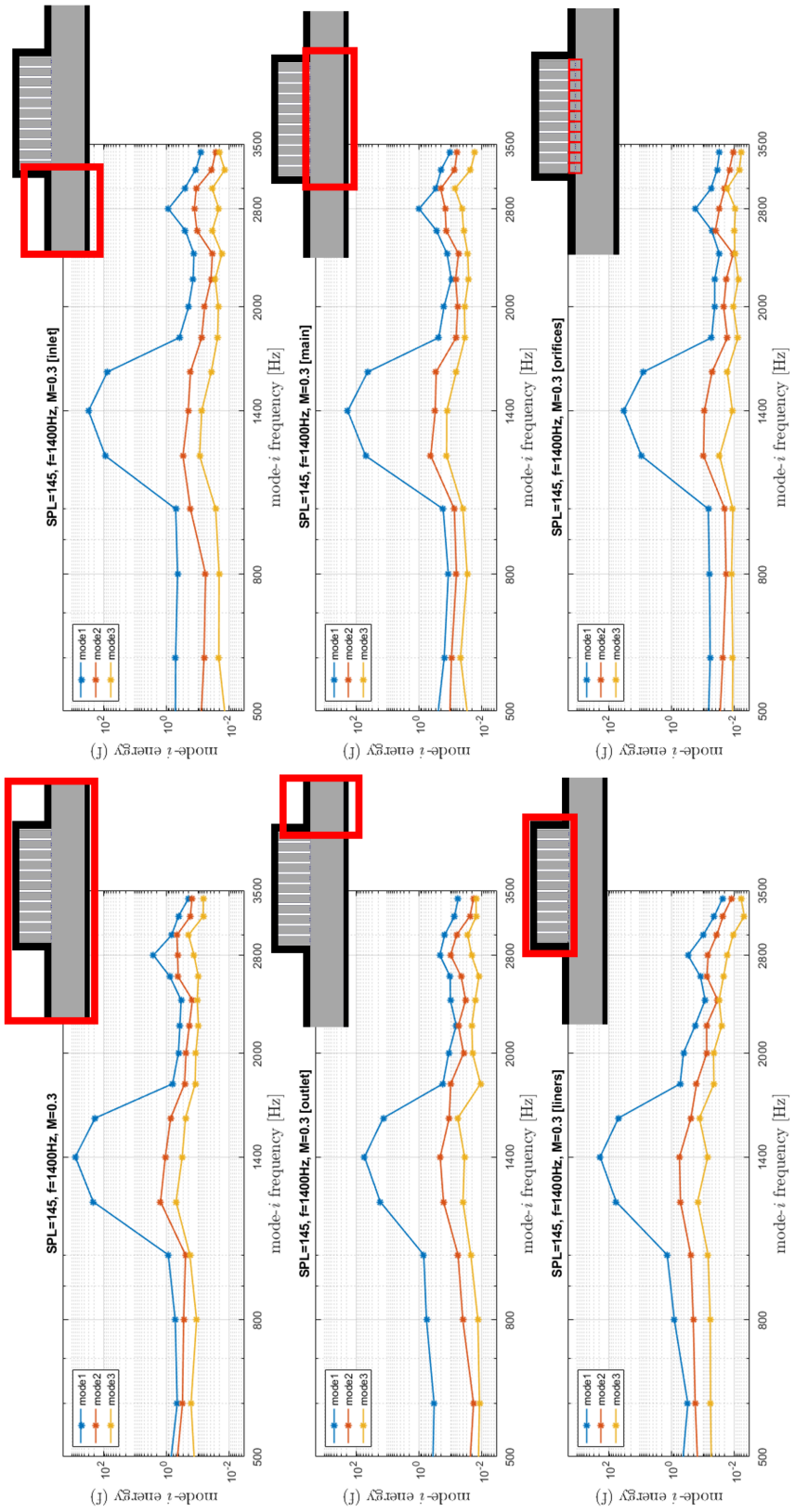

Fig. 4.32 $M = 0.3$: modal spectra. As well as for the no-flow condition, most part of the energy content is stored in the 1^{st} mode at the forcing wave frequency, and the second harmonic is barely distinguishable from other noise. While in the case of no-flow condition in outlet only the first mode survived, in this case energy content is still well distributed on higher order modes.

4.2.4 Modal Energies

The Modal Energies chart, represents the integrated energy content per each mode in each ROI. While for the $M = 0.3$ flow condition, Figure 4.33, apart from the first mode to dominate the scales, the other ones cover lower energy scales in a well distributed behavior in every ROI analyzed, and the decrease seems to cover all of the modes in equal manner. Unlike for the previous case, the energy distribution in outlet for the only-acoustics firstly increases the dominance of the first mode (behavior already observed in the spectra chart, Figure 4.31), and secondly the perception of a stronger damping is on several orders of magnitude greater than for the other examined case.

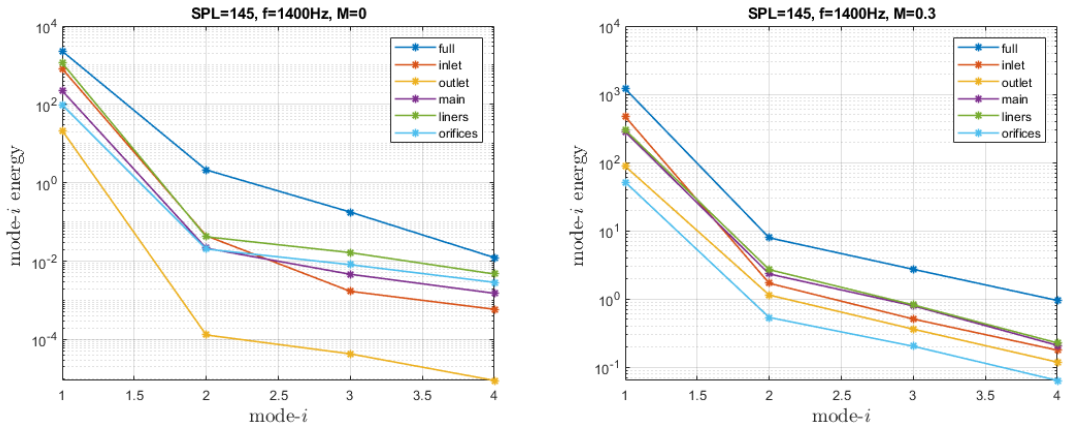

Fig. 4.33 modal energies.

4.2.5 Modal Comparison

In comparing only the first mode between the two experiments analyses, it is interesting to observe that while for *inlet* and main sections the spectra result very similar, the outlet presents a broader frequency content for the turbulent flow case experiment (apart from the lower attenuation).

One more interesting behavior is seen in the ROIs corresponding to the orifices and liners: while the absence of the flow admits the regular entrance of the modal energy in that regions, its presence limits this behavior, partly the non-linear regime is the cause of this as a “virtual” restriction of the orifices occurs by limiting the regular flow and partly occlusion occurs for the boundary layer and non-regular vortex shedding presence.

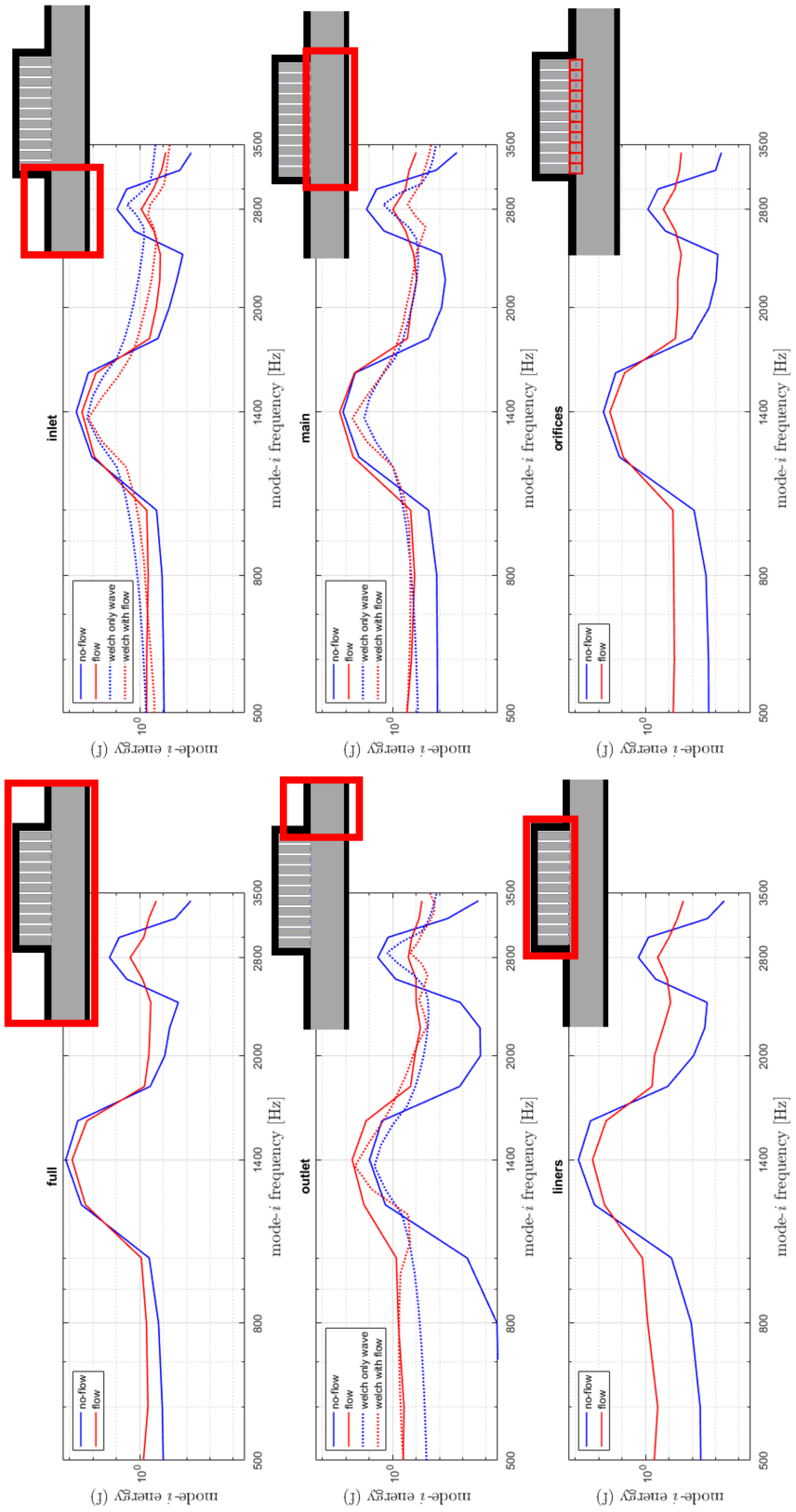

Fig. 4.34 SPOD: modal spectra comparison

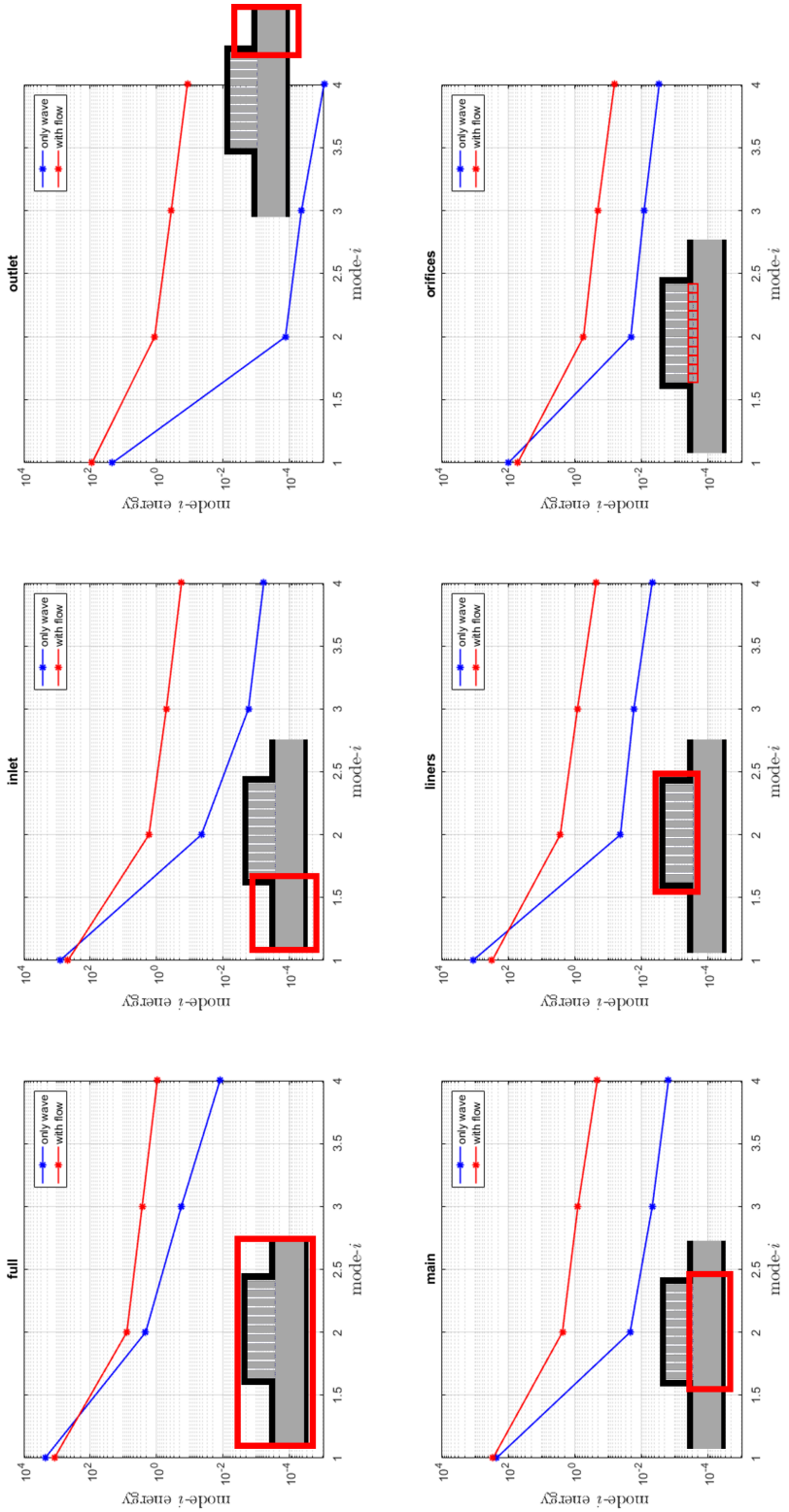

Fig. 4.35 SPOD: modal energies' comparison: for every ROI and mode number, apart from the liners and orifices areas (like already commented), the no-flow condition determines a more "dominant-only" behavior with a greater attenuation in all the modes and ROIs, in respect to the grazing flow case.

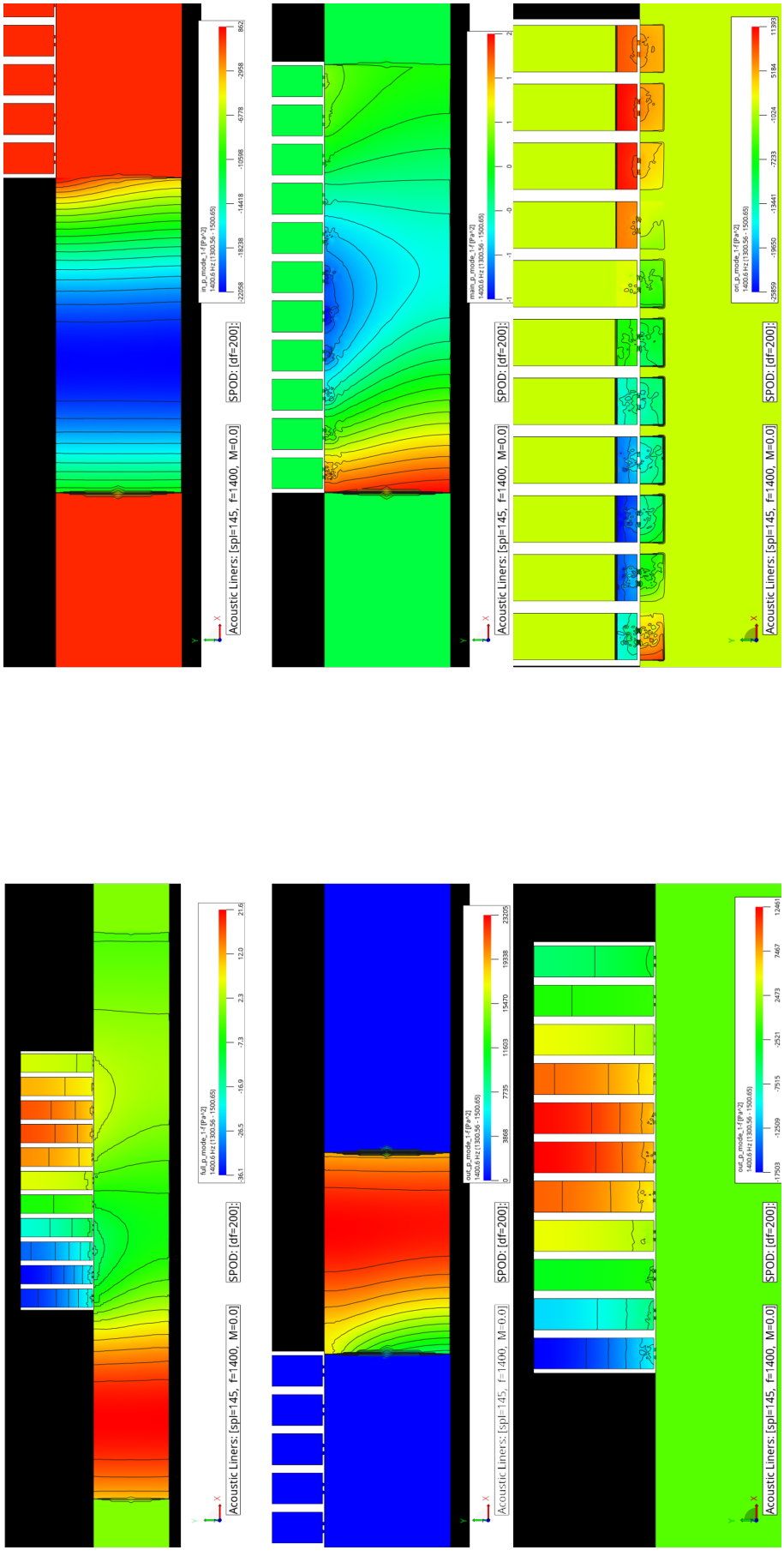

Fig. 4.36 $M = 0$: SPOD: modal spectra contour comparison at $f = 1400Hz$

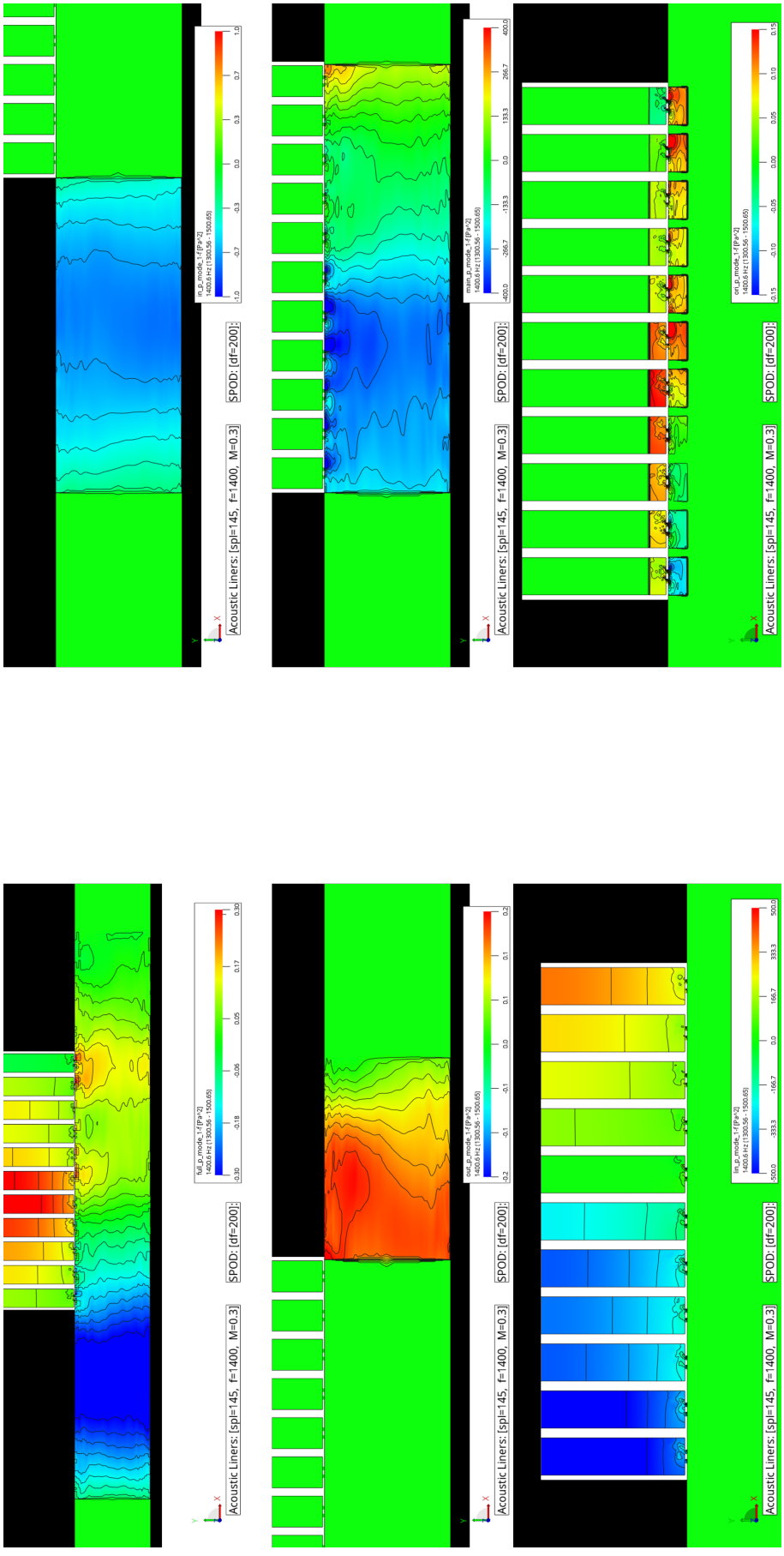

Fig. 4.37 $M = 0.3$: SPOD: modal spectra contour comparison at $f = 1400Hz$

4.3 Wavelet analysis

4.3.1 Output Data

The wavelet decomposition tool from "Opty-dB" relies its functioning on a wavelet transform-based method *WT1* [31], by splitting into Coherent and Gaussian content where the value of the threshold is calculated in an iterative way, according to the cross-correlation assumptions between the received "acoustic" signal by a microphone probe and the pressure fluctuations registered in a domain's point.

The main outputs of this wavelet analysis tool are SPL spectra for each contribution, coherent, gaussian and total. disposed on the set frequency bands. And the transient reconstruction based on this Coherent/Gaussian splitting.

From the SPL contours comparisons, it is very difficult to extrapolate some unequivocal judgments, but few aspects of the liners functioning are still observable.

4.3.2 Only Acoustics case

- The first useful information from the output data is that most of the acoustical energy is classified as coherent, because of the $WT1$ method used, and is almost exclusively present at the wave frequency $\approx 1400Hz$, which ranges from 120 to 147 dB, with a minimum zone located under the lasts liners in the array. After the liners area, the SPL content is almost constant at the value $\approx 130dB$, in agreement with the precedent spectral analysis. The firsts liners have to deal with greater amounts of acoustic energy, evidenced by the red zone $\approx 145dB$.

- The Gaussian content at the key frequency of $1400Hz$, results much lower than the same at the frequency of $\approx 411Hz$ (this frequency shift is observable also in the case of turbulent flow). Nevertheless, its content remains orders of magnitude below the coherent contributions.

- The orifices zoom-in view shows a high gaussian related power content, while the coherent has a regular passage of waves that after a short distance become plane wave propagation.

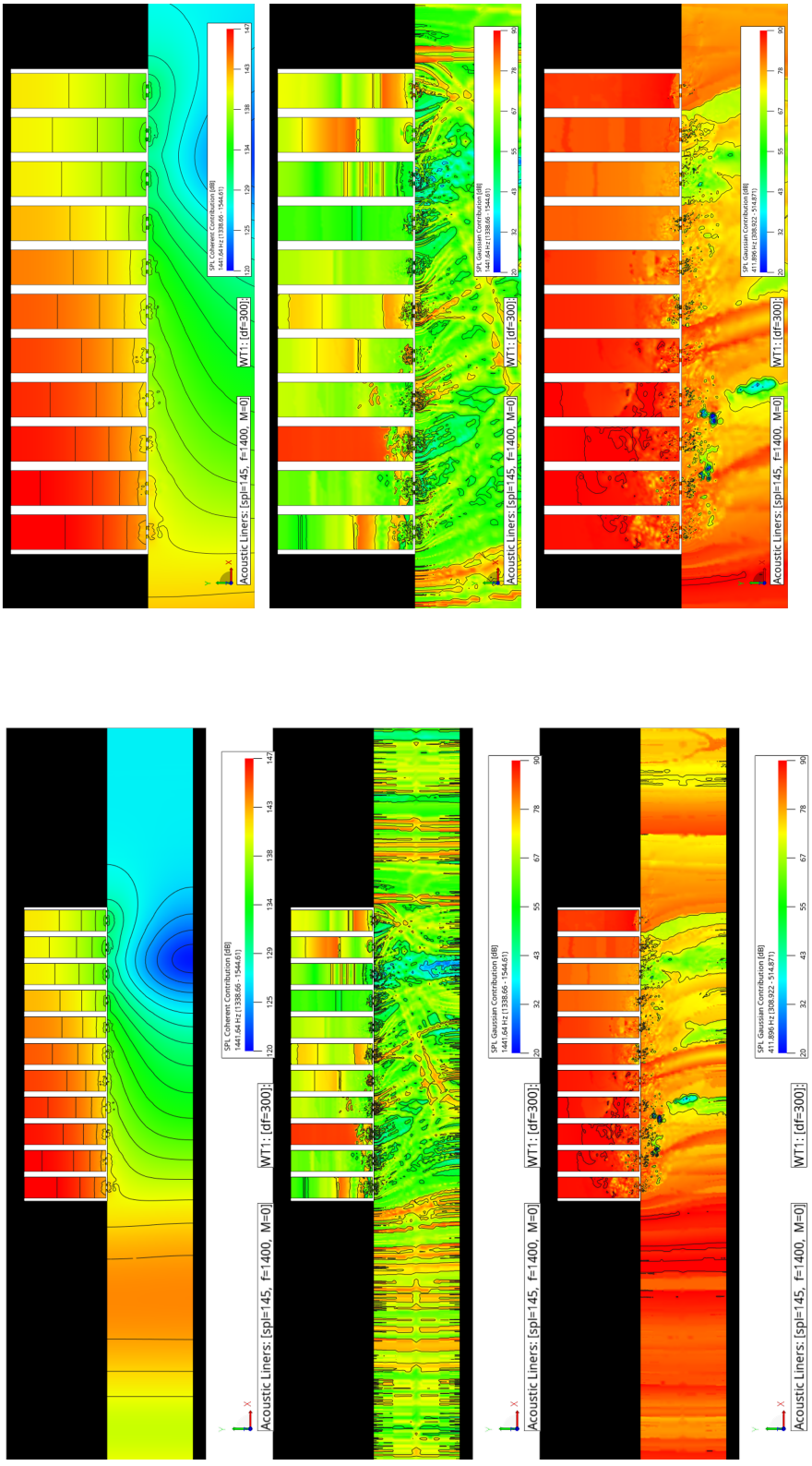

Fig. 4.38 Wavelet ($M = 0$): SPL contour comparison

4.3.3 Grazing Flow case

- The most interesting aspect in the case of flow presence is the maximum/minimum coherent contribution areas that form on the orifices edges and traces of vortex shedding occurrence right after it. Again, the most energy containing frequencies are those corresponding to the forcing wave, $f = 1400Hz$.
- As well as for the case of only-acoustic waves, the spectral content of the gaussian contribution is shifted to lower frequencies, $411Hz$, this frequency band (approximately $\pm 150Hz$) appears to contain more energy content than the lower one, $\approx 200Hz$.
- Due to the presence of the flow and the consequent Boundary layer formed, its presence is observable in the proximity of the walls only of the gaussian contribution.

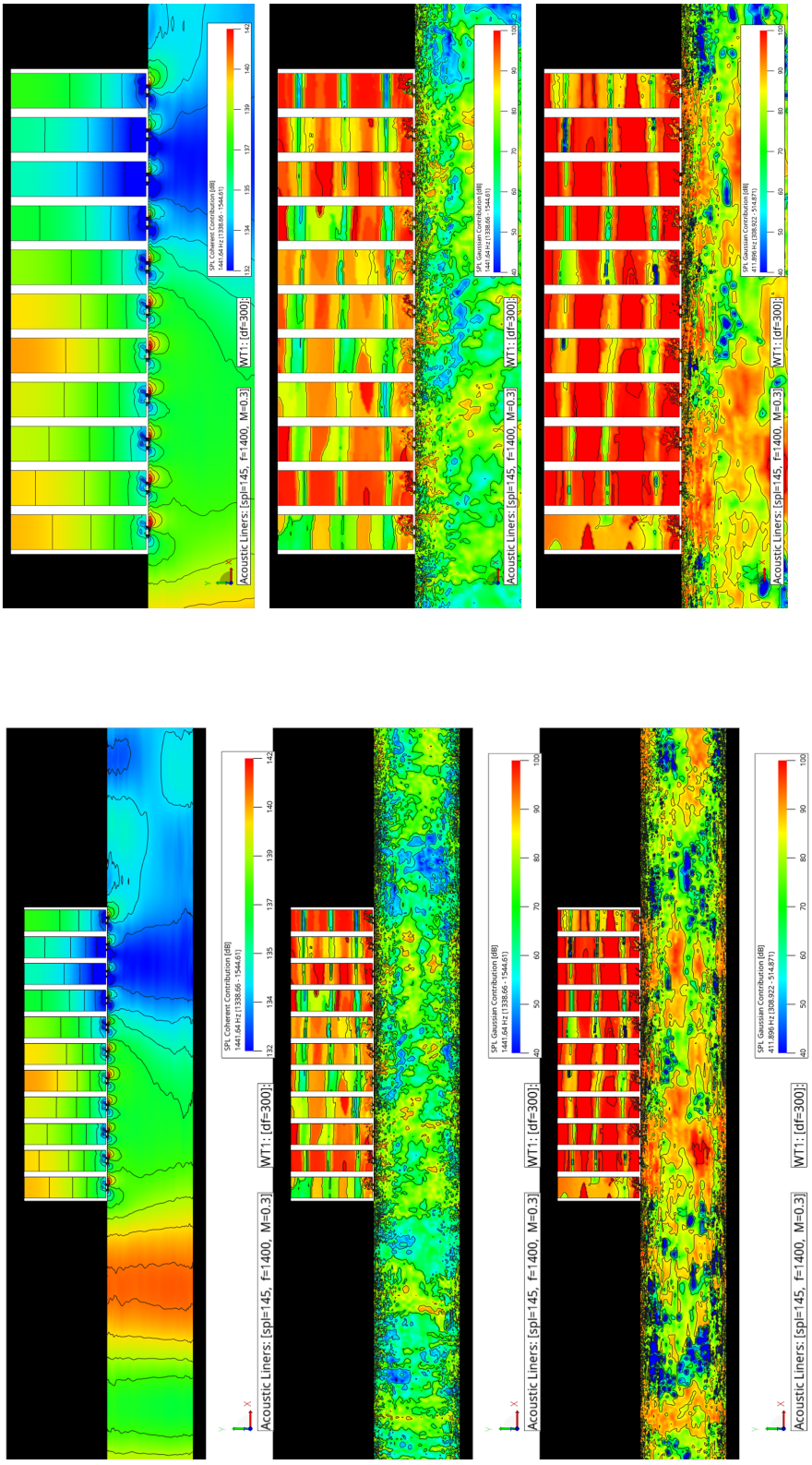

Fig. 4.39 Wavelet ($M = 03$): SPL contour comparison

Conclusions

Two solutions of a duct with a section facing an array of acoustic liners were analyzed with different techniques, the classical and the novel ones. While the lasts rely on not so recently introduced methods, these remained unfeasible until recent technological advancements.

Spectral Analysis The traditional spectral analysis tools remain a necessary first step for every subsequent analysis, independently of their nature and field of application. These analyses remain very flexible, easy to implement and offer a rapid introspection on possible "hidden" behaviors. Furthermore, these methods serve as the launchpad for any other operation. like in the examined case, spectral analysis was necessary for the correct setup of the successive SPOD and Wavelet analyses.

SPOD Analysis The Spectral Proper Orthogonal Decomposition application was examined and successfully applied to the test case of acoustic liners. Modal decomposition offers a great way to understand the behavior of highly energetic structures and phenomenons. The power and memory demand for its use remains an open issue, but with a proper preliminary study and a very localized applications, it is possible to minimize these "minimum" requirements. SPOD's use, with a more profound understanding, can become one of the basic tools for any kind of analyses, along with a "standard" spectral or others like the "classic" POD.

Wavelet Analysis The Wavelet Analysis remains the most recent of the adopted techniques. In fact, its algorithm and tool introductions were just recent to several months prior to its the application, and in consequence present less flexibility in comparison to the other adopted techniques. Nevertheless, even being novel, it offers an alternative point of view with different possibilities in comparison to the other common methods. Certainly, with a more profound understanding, it can reveal useful aspects of the dynamics involved in aeroacoustically perturbed flow fields.

References

[1] Renzo Arina. Appunti del corso di aeroacustica. In *Aeroacustica*, 2022. materiale messo a disposizione ad uso esclusivo degli studenti del corso di Aeroacustica per la Laurea Magistrale in Ingegneria Aerospaziale del Politecnico di Torino.

[2] Julius S. Bendat and Allan G. Piersol. *Random Data: Analysis and Measurement Procedures*, 1987. URL https://api.semanticscholar.org/CorpusID:109797040.

[3] Steven L. Brunton and J. Nathan Kutz. *Data-Driven Science and Engineering: Machine Learning, Dynamical Systems, and Control*. Cambridge University Press, 2019. doi: 10.1017/9781108380690.

[4] R. Camussi and G. Guj. Orthonormal wavelet decomposition of turbulent flows: intermittency and coherent structures. *Journal of Fluid Mechanics*, 348:177–199, 1997. doi: 10.1017/S0022112097006551.

[5] Damiano Casalino and Mattia Barbarino. Optimization of a single-slotted lined flap for wing trailing-edge noise reduction. *Journal of Aircraft*, 49(4):1051–1063, 2012. doi: 10.2514/1.C031561. URL https://doi.org/10.2514/1.C031561.

[6] W. Cazemier, R. W. C. P. Verstappen, and A. E. P. Veldman. Proper orthogonal decomposition and low-dimensional models for driven cavity flows. *Physics of Fluids*, 10(7):1685–1699, 07 1998. ISSN 1070-6631. doi: 10.1063/1.869686. URL https://doi.org/10.1063/1.869686.

[7] Tim Colonius and Kunihiko Taira. A fast immersed boundary method using a nullspace approach and multi-domain far-field boundary conditions. *Computer Methods in Applied Mechanics and Engineering*, 197(25):2131–2146, 2008. ISSN 0045-7825. doi: https://doi.org/10.1016/j.cma.2007.08.014. URL https://www.sciencedirect.com/science/article/pii/S0045782507003362. Immersed Boundary Method and Its Extensions.

[8] N. Curle and Michael James Lighthill. The influence of solid boundaries upon aerodynamic sound. *Proceedings of the Royal Society of London. Series A. Mathematical and Physical Sciences*, 231(1187):505–514, 1955. doi: 10.1098/rspa.1955.0191. URL https://royalsocietypublishing.org/doi/abs/10.1098/rspa.1955.0191.

[9] Ingrid Daubechies. *Ten Lectures on Wavelets*. Society for Industrial and Applied Mathematics, 1992. doi: 10.1137/1.9781611970104. URL https://epubs.siam.org/doi/abs/10.1137/1.9781611970104.

[10] David L. Donoho and Iain M. Johnstone. Ideal spatial adaptation by wavelet shrinkage. *Biometrika*, 81(3):425–455, 1994. ISSN 00063444. URL http://www.jstor.org/stable/2337118.

[11] Marie Farge. Wavelet transforms and their applications to turbulence. *Annual Review of Fluid Mechanics*, 24(1):395–458, 1992. doi: 10.1146/annurev.fl.24.010192.002143. URL https://doi.org/10.1146/annurev.fl.24.010192.002143.

[12] J. E. Ffowcs Williams, D. L. Hawkings, and Michael James Lighthill. Sound generation by turbulence and surfaces in arbitrary motion. *Philosophical Transactions of the Royal Society of London. Series A, Mathematical and Physical Sciences*, 264(1151):321–342, 1969. doi: 10.1098/rsta.1969.0031. URL https://royalsocietypublishing.org/doi/abs/10.1098/rsta.1969.0031.

[13] Karl Pearson F.R.S. Liii. on lines and planes of closest fit to systems of points in space. *Philosophical Magazine Series 1*, 2:559–572, 1901. URL https://api.semanticscholar.org/CorpusID:125037489.

[14] William K. George, Paul Douglas Beuther, and John L. Lumley. *Processing of Random Signals*, 1978. URL https://api.semanticscholar.org/CorpusID:109474553.

[15] S. Grizzi and R. Camussi. Wavelet analysis of near-field pressure fluctuations generated by a subsonic jet. *Journal of Fluid Mechanics*, 698:93–124, 2012. doi: 10.1017/jfm.2012.64.

[16] A.W. Guess. Calculation of perforated plate liner parameters from specified acoustic resistance and reactance. *Journal of Sound and Vibration*, 40(1):119–137, 1975. ISSN 0022-460X. doi: https://doi.org/10.1016/S0022-460X(75)80234-3. URL https://www.sciencedirect.com/science/article/pii/S0022460X75802343.

[17] Alfred Haar. Zur theorie der orthogonalen funktionensysteme. *Mathematische Annalen*, 69, 1910. doi: 10.1007/BF01456326. URL https://doi.org/10.1007/BF01456326.

[18] Philip Holmes, John L. Lumley, Gahl Berkooz, and Clarence W. Rowley. *Turbulence, Coherent Structures, Dynamical Systems and Symmetry*. Cambridge Monographs on Mechanics. Cambridge University Press, 2 edition, 2012. doi: 10.1017/CBO9780511919701.

[19] Harold Hotelling. Analysis of a complex of statistical variables into principal components. *Journal of Educational Psychology*, 24:498–520, 1933. URL https://api.semanticscholar.org/CorpusID:144828484.

[20] M. S. Howe. *Acoustics of Fluid-Structure Interactions*. Cambridge Monographs on Mechanics. Cambridge University Press, 1998. doi: 10.1017/CBO9780511662898.

[21] Uno Ingard. On the theory and design of acoustic resonators. *The Journal of the Acoustical Society of America*, 25(6):1037–1061, 11 1953. ISSN 0001-4966. doi: 10.1121/1.1907235. URL https://doi.org/10.1121/1.1907235.

[22] Christopher Jasinski and Thomas Corke. Mechanism for increased viscous drag over porous sheet acoustic liners. *AIAA Journal*, 58(8):3393–3404, 2020. doi: 10.2514/1.J059039. URL https://doi.org/10.2514/1.J059039.

[23] Michael Jones, Maureen Tracy, Willie Watson, and Tony Parrott. Effects of liner geometry on acoustic impedance. In *8th AIAA/CEAS Aeroacoustics Conference & Exhibit*, 2002. doi: 10.2514/6.2002-2446. URL https://arc.aiaa.org/doi/abs/10.2514/6.2002-2446.

[24] Michael Jones, Willie Watson, Douglas Nark, Brian Howerton, and Martha Brown. *A Review of Acoustic Liner Experimental Characterization at NASA Langley*, 04 2020.

[25] Takeo Kajishima and Kunihiko Taira. *Computational Fluid Dynamics*. Springer International Publishing, 2017. ISBN 978-3-319-45304-0. URL https://doi.org/10.1007/978-3-319-45304-0.

[26] Andrew Kempton. Acoustic liners for modern aero-engines. In *Rolls-Royce plc*, 2011. URL https://www.win.tue.nl/ceas-asc/Workshop15/CEAS-ASC_XNoise-EV_K1_Kempton.pdf.

[27] Franck Kerhervé, Antoine Guitton, Peter Jordan, J. Delville, Véronique Fortuné, Yves Gervais, and Charles E. Tinney. Identifying the dynamics underlying the large-scale and fine-scale jetnoise similarity spectra. In ., 2008.

[28] A. Kierkegaard, E. Åkervik, G. Efraimsson, and D.S. Henningson. Flow field eigenmode decompositions in aeroacoustics. *Computers & Fluids*, 39(2):338–344, 2010. ISSN 0045-7930. doi: https://doi.org/10.1016/j.compfluid.2009.09.010. URL https://www.sciencedirect.com/science/article/pii/S0045793009001352.

[29] Michael James Lighthill and Maxwell Herman Alexander Newman. On sound generated aerodynamically i. general theory. *Proceedings of the Royal Society of London. Series A. Mathematical and Physical Sciences*, 211(1107):564–587, 1952. doi: 10.1098/rspa.1952.0060. URL https://royalsocietypublishing.org/doi/abs/10.1098/rspa.1952.0060.

[30] John L. Lumley. The structure of inhomogeneous turbulent flows. *Atmospheric Turbulence and Radio Propagation*, pages 166–178, 1967.

[31] Matteo Mancinelli, Tiziano Pagliaroli, Alessandro Di Marco, Roberto Camussi, and Thomas Castelain. Wavelet decomposition of hydrodynamic and acoustic pressures in the near field of the jet. *Journal of Fluid Mechanics*, 813:716–749, 2017. doi: 10.1017/jfm.2016.869.

[32] T. H. Melling. The acoustic impedance of perforates at medium and high sound pressure levels. *Journal of Sound and Vibration*, 29:1–65, 1973.

[33] Yves Meyer. *Wavelets and Operators*. Cambridge Studies in Advanced Mathematics. Cambridge University Press, 1993.

[34] H. K. Moffatt. Stochastic tools in turbulence. by john l. lumley. academic press, 1970. 205 pp. *Journal of Fluid Mechanics*, 67(2):413–415, 1975. doi: 10.1017/S0022112075210389.

[35] J. Morlet. Sampling theory and wave propagation. In C. H. Chen, editor, *Issues in Acoustic Signal — Image Processing and Recognition*, pages 233–261, Berlin, Heidelberg, 1983. Springer Berlin Heidelberg. ISBN 978-3-642-82002-1.

[36] R.E. Motsinger and R.E. Kraft. *Design and Performance of Duct Acoustic Treatment*, volume 2: Noise Control, chapter 14. National Aeronautics and Space Administration, Langley Research Center Hampton, Virginia, United States, 1991.

[37] Bernd R. Noack, Paul Papas, and Peter A. Monkewitz. The need for a pressure-term representation in empirical galerkin models of incompressible shear flows. *Journal of Fluid Mechanics*, 523:339–365, 2005. doi: 10.1017/S0022112004002149.

[38] Angelo Paduano. *Acoustic liner literature review*, 2023.

[39] C. Picard and J. Delville. Pressure velocity coupling in a subsonic round jet. *International Journal of Heat and Fluid Flow*, 21(3):359–364, 2000. ISSN 0142-727X. doi: https://doi.org/10.1016/S0142-727X(00)00021-7. URL https://www.sciencedirect.com/science/article/pii/S0142727X00000217.

[40] Leandro Rego, Francesco Avallone, Daniele Ragni, and Damiano Casalino. On the mechanisms of jet-installation noise reduction with flow-permeable trailing edges. *Journal of Sound and Vibration*, 520:116582, 2022. ISSN 0022-460X. doi: https://doi.org/10.1016/j.jsv.2021.116582. URL https://www.sciencedirect.com/science/article/pii/S0022460X21006003.

[41] Leandro Rego, Francesco Avallone, Daniele Ragni, Damiano Casalino, and Hervé Denayer. Acoustic liners for jet-installation noise reduction. *Journal of Sound and Vibration*, 537:117189, 2022. ISSN 0022-460X. doi: https://doi.org/10.1016/j.jsv.2022.117189. URL https://www.sciencedirect.com/science/article/pii/S0022460X22003856.

[42] Risorse di calcolo fornite da HPC@POLITO, progetto di Academic Computing del Dipartimento di Automatica e Informatica presso il Politecnico di Torino. *Computing Power*, 2024. URL http://www.hpc.polito.it.

[43] Clarence W. Rowley, Tim Colonius, and Richard M. Murray. Model reduction for compressible flows using pod and galerkin projection. *Physica D: Nonlinear Phenomena*, 189(1):115–129, 2004. ISSN 0167-2789. doi: https://doi.org/10.1016/j.physd.2003.03.001. URL https://www.sciencedirect.com/science/article/pii/S0167278903003841.

[44] Jori Ruppert-Felsot, Marie Farge, and Philippe Petitjeans. Wavelet tools to study intermittency: application to vortex bursting. *Journal of Fluid Mechanics*, 636:427–453, 2009. doi: 10.1017/S0022112009008003.

[45] Oliver T. Schmidt and Tim Colonius. Guide to spectral proper orthogonal decomposition. *AIAA Journal*, 58(3):1023–1033, 2020. doi: 10.2514/1.J058809. URL https://doi.org/10.2514/1.J058809.

[46] Oliver T. Schmidt and Aaron Towne. An efficient streaming algorithm for spectral proper orthogonal decomposition. *Computer Physics Communications*, 237:98–109, 2019. ISSN 0010-4655. doi: https://doi.org/10.1016/j.cpc.2018.11.009. URL https://www.sciencedirect.com/science/article/pii/S0010465518304016.

[47] Moritz Sieber, C. Oliver Paschereit, and Kilian Oberleithner. Spectral proper orthogonal decomposition. *Journal of Fluid Mechanics*, 792:798–828, 2016. doi: 10.1017/jfm.2016.103.

[48] Lawrence Sirovich. Turbulence and the dynamics of coherent structures. i. coherent structures. *Quarterly of Applied Mathematics*, 45:561–571, 10 1987. doi: 10.1090/qam/910462.

[49] Kunihiko Taira and Tim Coonius. Three-dimensional flows around low-aspect-ratio flat-plate wings at low reynolds numbers. *Journal of Fluid Mechanics*, 623:187–207, 2009. doi: 10.1017/S0022112008005314.

[50] Kunihiko Taira, Steven L. Brunton, Scott T. M. Dawson, Clarence W. Rowley, Tim Colonius, Beverley J. McKeon, Oliver T. Schmidt, Stanislav Gordeyev, Vassilios Theofilis, and Lawrence S. Ukeiley. Modal analysis of fluid flows: An overview. *AIAA Journal*, 55(12):4013–4041, 2017. doi: 10.2514/1.J056060. URL https://doi.org/10.2514/1.J056060.

[51] Christopher K. W. Tam and Konstantin A. Kurbatskii. Microfluid dynamics and acoustics of resonant liners. *AIAA Journal*, 38(8):1331–1339, 2000. doi: 10.2514/2.1132. URL https://doi.org/10.2514/2.1132.

[52] C. E. Tinney and P. Jordan. The near pressure field of co-axial subsonic jets. *Journal of Fluid Mechanics*, 611:175–204, 2008. doi: 10.1017/S0022112008001833.

[53] Aaron Towne, Oliver T. Schmidt, and Tim Colonius. Spectral proper orthogonal decomposition and its relationship to dynamic mode decomposition and resolvent analysis. *Journal of Fluid Mechanics*, 847:821–867, 2018. doi: 10.1017/jfm.2018.283.

[54] P. Welch. The use of fast fourier transform for the estimation of power spectra: A method based on time averaging over short, modified periodograms. *IEEE Transactions on Audio and Electroacoustics*, 15(2):70–73, June 1967. ISSN 1558-2582. doi: 10.1109/TAU.1967.1161901.

[55] Qi Zhang and Daniel J. Bodony. Numerical investigation of a honeycomb liner grazed by laminar and turbulent boundary layers. *Journal of Fluid Mechanics*, 792:936–980, 2016. doi: 10.1017/jfm.2016.79.